J. Fluid Mech. (2014), *vol.* 755, *pp.* 365–396.
doi:10.1017/jfm.2014.421

Internal stresses and breakup of rigid isostatic aggregates in homogeneous and isotropic turbulence

Jeremias De Bona[1], Alessandra S. Lanotte[2] and Marco Vanni[1,†]

[1]Dipartimento di Scienza Applicata e Tecnologia, Politecnico di Torino, Corso Duca degli Abruzzi 24, 10129 Torino, Italy

[2]CNR-ISAC, Istituto di Scienze dell'Atmosfera e del Clima, and INFN, Sezione di Lecce, Strada Provinciale Lecce–Monteroni, 73100 Lecce, Italy

(Received 18 November 2013; revised 29 April 2014; accepted 21 July 2014; first published online 19 August 2014)

By characterising the hydrodynamic stresses generated by statistically homogeneous and isotropic turbulence in rigid aggregates, we estimate theoretically the rate of turbulent breakup of colloidal aggregates and the size distribution of the formed fragments. The adopted method combines direct numerical simulation of the turbulent field with a discrete element method based on Stokesian dynamics. In this way, not only is the mechanics of the aggregate modelled in detail, but the internal stresses are evaluated while the aggregate is moving in the turbulent flow. We examine doublets and cluster–cluster isostatic aggregates, where the failure of a single contact leads to the rupture of the aggregate and breakup occurs when the tensile force at a contact exceeds the cohesive strength of the bond. Owing to the different role of the internal stresses, the functional relationship between breakup frequency and turbulence dissipation rate is very different in the two cases. In the limit of very small and very large values, the frequency of breakup scales exponentially with the turbulence dissipation rate for doublets, while it follows a power law for cluster–cluster aggregates. For the case of large isostatic aggregates, it is confirmed that the proper scaling length for maximum stress and breakup is the radius of gyration. The cumulative fragment distribution function is nearly independent of the mean turbulence dissipation rate and can be approximated by the sum of a small erosive component and a term that is quadratic with respect to fragment size.

Key words: particle/fluid flow, suspensions

1. Introduction

The dispersion of particles in a liquid, as performed in the compounding step of materials processing, involves the breakup of solid aggregates by hydrodynamic stresses. In addition, breakup plays an important role in many aggregation processes, where solid particles coagulate under the effect of mechanical stirring, and the final size distribution is often determined by the balance between aggregation of the smaller

† Email address for correspondence: marco.vanni@polito.it

particles and rupture of the larger ones. The two processes are frequently conducted under intense agitation, and in this case the hydrodynamic stress required for breakup is provided by turbulence.

In turbulent breakup, the complex dynamics of turbulence interacts with the intricate morphology of the aggregates, since it is the redistribution of the hydrodynamic force over the structure of the aggregate that may cause the stress to accumulate in some critical locations and exceed the cohesive strength. Hence, it is not surprising that, despite considerable efforts, a basic understanding of breakup dynamics in turbulent flows is still lacking.

So far, the methods for the study of breakup have proceeded along two main lines. One approach aims at predicting accurately the hydrodynamic stresses in the aggregate in simple flow fields, such as shear or elongational flow. Initially these studies were performed on highly idealised aggregates with spherical symmetry and uniform porosity (Adler & Mills 1979), or radially decreasing porosity (Sonntag & Russel 1987), and by using Brinkman's equation to model the flow in the porous region. Subsequently, Horwatt, Feke & Manas-Zloczower (1992*a*) and Horwatt, Manas-Zloczower & Feke (1992*b*) made it apparent that the simulation of the stress distribution had to be based on more realistic reproductions of the aggregates, because weak points or local heterogeneities in the structure, which are not captured by idealised representations, play a fundamental role in starting breakup. This consideration led to the application of discrete element methods (DEMs), which model in detail the disordered structure of the aggregates and take into account the effect that each primary particle has in generating and transmitting stress. Different techniques were employed to estimate hydrodynamic forces in DEMs, including free-draining approximation (Potanin 1993; Becker *et al.* 2009; Eggersdorfer *et al.* 2010), simplified hydrodynamic screening models (Higashitani & Iimura 1998; Higashitani, Iimura & Sanda 2001; Fanelli, Feke & Manas-Zloczower 2006), method of reflections (Gastaldi & Vanni 2011) and Stokesian dynamics (Harada *et al.* 2006; Seto, Botet & Briesen 2011; Vanni & Gastaldi 2011; Harshe & Lattuada 2012). DEMs allow the estimation of the strength of the flow field required to break a given aggregate. Usually such results are summarised in terms of a breakup exponent m that relates the size of the aggregate, d, with the critical shear rate needed to break it, $\dot{\gamma}_{cr}$, which was found to depend on aggregate morphology (Zaccone *et al.* 2009):

$$d \propto \dot{\gamma}_{cr}^{-m}. \tag{1.1}$$

Empirical studies and semi-theoretical analyses based on simplified energy balances (Parker, Kaufmann & Jenkins 1972; Kobayashi, Adachi & Doi 1999; Bache 2004; Wengeler & Nirschl 2007) suggest that (1.1) also estimates the size of the aggregates resulting from a process of turbulent breakup, provided that the effective mean shear rate for the turbulent flow is used:

$$\dot{\gamma}_{eff} = \sqrt{\langle \varepsilon \rangle / \nu}, \tag{1.2}$$

where $\langle \varepsilon \rangle$ is the mean kinetic energy dissipation rate and ν is the fluid kinematic viscosity.

Whereas laminar shear flows are characterised by a single value of shear rate, in a turbulent flow $\dot{\gamma}_{eff}$ is the outcome of a wide distribution of instantaneous and local shear rates. Hence, the occurrence of a value of such a shear rate strong enough to induce breakup obeys a statistical spatial and temporal distribution dictated by the turbulence. In order to take this effect into account, the study of turbulent breakup

normally followed a different approach, which was aimed at the prediction of the breakup rate and did not consider the details of the structure of the aggregates.

The rate of turbulent breakup for particles of a given size d is the number of such particles that undergo rupture per unit time and per unit volume of suspension. It can be expressed as $f_{br}(d)n(d)$, where $n(d)$ is the number concentration of the particles and $f_{br}(d)$ is called the breakup frequency or, in the field of population balances, the breakup kernel (Vanni 2000*a*; Marchisio & Fox 2013). The simplest models for the breakup frequency (Pandya & Spielman 1983; Lu & Spielman 1985; Spicer & Pratsinis 1996) prescribe a power-law relationship in terms of shear rate and aggregate size:

$$f_{br}(d) \propto \dot{\gamma}_{eff}^{\alpha} d^{\beta}, \tag{1.3}$$

where α and β are positive empirical parameters that account for the fact that breakup is faster for larger aggregates and for stronger turbulence. A more theoretical approach was developed by Kusters (1991), who assumed that in a homogeneous turbulent system, where the hydrodynamic field is continuously changing in time, breakup occurs whenever the local instantaneous velocity gradient around the aggregate exceeds the critical value given by (1.1). Hence, the breakup rate is determined by the frequency at which the shear rate becomes larger than $\dot{\gamma}_{cr}$ (Delichatsios 1975). By assuming a normal distribution for the local shear rate (Delichatsios & Probstein 1976), the breakup frequency of small particles results in the following expression:

$$f_{br}(d) = \sqrt{\frac{4\langle\varepsilon\rangle}{15\pi\nu}}\, \exp\left(-\frac{15}{2}\frac{\nu}{\langle\varepsilon\rangle}[\dot{\gamma}_{cr}(d)]^2\right). \tag{1.4}$$

A similar point of view was adopted by Bäbler and co-workers, who characterised turbulence by a multifractal model (Bäbler, Morbidelli & Baldyga 2008) and proposed a breakup rate function that is equal to (1.4) for small aggregates, while it becomes a power law in the limit of very large ones. In a subsequent work, Bäbler, Biferale & Lanotte (2012) adopted first-passage-time statistics (Redner 2001) to estimate the breakup rate by means of direct numerical simulation (DNS) data. Moreover, they showed that an Eulerian proxy, based on the joint statistics of the instantaneous energy dissipation and its time derivative, can alternatively be used, since it is easier to measure in experiments.

The previous approaches consider separately the roles of turbulence and aggregate mechanics. Aggregate mechanics and the behaviour in simple flow fields set the relationship between aggregate size and critical strain rate, $\dot{\gamma}_{cr}(d)$, whereas turbulence determines the functional relationship between the breakup frequency of an aggregate and its critical strain rate, $f_{br}(\dot{\gamma}_{cr})$. However, the ability of the local flow field to break an aggregate may depend not only on the strength of the flow $\dot{\gamma}$, but also on the instantaneous orientation of the particle with respect to the flow field and hence on the history of the aggregate. A certain value of $\dot{\gamma}$ can break an aggregate if its orientation enhances internal stresses, but may not be sufficient in the case of unfavourable alignment. This implies an interaction between mechanical and fluid dynamic aspects, and considering them separately, as done in the aforementioned approaches, may not be accurate, particularly in the case of small aggregates.

The method used here combines DNS of the turbulent field with a DEM based on Stokesian dynamics, which models in detail the mechanics of the aggregate and evaluates internal stresses while the aggregate is moving in the turbulent field. The adopted DEM approach is a refinement of the method used previously by Vanni and

co-workers (Vanni & Gastaldi 2011; Sanchez Fellay & Vanni 2012) for steady laminar flow fields.

The breakup frequency is estimated by using the approach devised by Bäbler *et al.* (2012) to process data from the DNS of turbulence. However, Bäbler *et al.*'s method does not take into account the effect of the structure on the redistribution of the internal stresses inside the aggregates and assumes that an aggregate breaks up whenever its critical flow strength $\dot{\gamma}_{cr}$ is exceeded. On the contrary, in our case, breakup is assumed to occur when the internal stress on the most loaded inter-monomer bond exceeds the cohesive force of the bond. In this way, the effect of aggregate orientation on stress distribution and, consequently, on breakup is implicitly taken into account.

So far, simulations that capture in detail both the fluid dynamic and the mechanical aspects of the problem for a turbulent system have been restricted to doublets, that is, rigid aggregates formed by two contacting spherical monomers. In Derksen (2008), the problem was solved numerically for particles with size slightly larger than the Kolmogorov length scale by calculating very precisely the flow field around the particles with a lattice-Boltzmann method. Such an approach is not practicable for studying aggregates made by many monomers or smaller than the Kolmogorov length scale, owing to the exceedingly high computational cost of the method. From this point of view, the combination of DNS and Stokesian dynamics, although less accurate, provides an excellent alternative and allowed us to investigate the behaviour of aggregates that are more typical of the colloidal domain.

In the first part of the work, we discuss the results obtained in the simulation of doublets, where the physical interpretation of the simulation is easier because of the simple geometry. In the second part, we present the results for more realistic rigid cluster–cluster (CC) aggregates of low fractal dimension made by several hundred primary particles. Throughout the work, we consider isostatic aggregates, that is, clusters without redundant bonds, where the failure of a single contact always leads to the breakup of the structure. At a physical level, aggregates with such features are normally obtained by aggregation of highly destabilised colloidal suspensions, in which most collisions lead to permanent bonds and no restructuring of the structure has occurred (Gastaldi & Vanni 2011).

The two aforementioned cases of doublets and large CC aggregates are the extreme conditions of a range of situations. As shown in the following sections, the doublet is the system for which the effect of orientation is highest, since the single contact of this configuration is subject to alternating traction and compression. Differently, this effect is significantly reduced with large CC aggregates, where there are bonds under traction under any possible orientation, owing to their large and disordered structure.

2. Methods

2.1. *Main assumptions*

We investigate the breakup of small aggregates induced by stationary homogeneous and isotropic turbulence in dilute suspensions. In this case the finest structures of turbulence can be characterised by Kolmogorov length scale η_k and time scale τ_k, defined as

$$\eta_k = (\nu^3/\langle\varepsilon\rangle)^{1/4}, \tag{2.1}$$

$$\tau_k = (\nu/\langle\varepsilon\rangle)^{1/2}. \tag{2.2}$$

We assume that the aggregates are much smaller than the scale of the smallest turbulent motions, $(d/\eta_k) \ll 1$. This condition implies that the aggregate Reynolds number Re_p is very small, too:

$$Re_p = \frac{\dot{\gamma}_{eff} d^2}{\nu} = \left(\frac{d}{\eta_k}\right)^2. \tag{2.3}$$

Consequently, the aggregate is moving under creeping flow conditions. The aggregate relaxation time is $\tau_r = (2\varrho_p/\varrho_f + 1)d^2/(36\nu)$ and the Stokes number results in:

$$St_p = \frac{\tau_r}{\tau_k} = \frac{2\varrho_p/\varrho_f + 1}{36} Re_p. \tag{2.4}$$

For solid–liquid dispersions, $\varrho_p/\varrho_f \sim 1$ and $St_p \ll 1$, the response of the particles to changes in the flow field is very fast, confirming that the inertia of aggregates is negligible.

The previous assumptions are normally fulfilled in the turbulent breakup of dilute solid–liquid colloidal dispersions. In this case, the size of the aggregates is less than a few micrometres, whereas η_k is seldom below 50 μm for mechanically stirred suspensions. Hence, at all times these aggregates see a smooth and spatially well correlated flow field around them. In such flow, the local turbulent dissipation rate is related to the shear rate by the relationship

$$\varepsilon = \nu\dot{\gamma}^2. \tag{2.5}$$

The shear rate is a function of the spatial velocity derivatives through the rate-of-strain tensor e_{ij}^{∞}:

$$\dot{\gamma} = \sqrt{2e_{ij}^{\infty} e_{ij}^{\infty}} \quad \text{and} \quad e_{ij}^{\infty} = \frac{1}{2}\left(\frac{\partial u_i}{\partial x_j} + \frac{\partial u_j}{\partial x_i}\right). \tag{2.6a,b}$$

In fully developed turbulent flow, the local energy dissipation rate is a highly fluctuating quantity. While the internal stresses acting on the aggregate are determined by the interaction of the aggregate structure with the flow field in its closest neighbourhood, the rate of breakup depends also on the probability to enter a region of high strain and hence on the motion of the aggregate over larger scales. To capture both aspects, the numerical investigation was performed at two different levels. The fluid dynamics at the scales comparable to and larger than the Kolmogorov length scale and the trajectories of the particles were calculated by a DNS of the turbulent flow, in which the aggregates were modelled as point tracer particles, owing to their small size in comparison to the relevant turbulent scales and their negligible inertia. Then, Stokesian dynamics was adopted to evaluate the phenomena governed by the smooth velocity field at the scales smaller than η_k. Thanks to the information on the velocity gradients at the location of the aggregates provided by the DNS, and by taking into account the actual geometry of the particles, Stokesian dynamics predicted both the rotational component of the motion of the aggregates and the hydrodynamic forces acting on all monomers. From this type of information, it is possible to evaluate the internal forces and torques acting at inter-monomer contacts and determine the occurrence of breakup. As the aggregates studied in this work are rigid and isostatic, rupture is caused by the failure of a single inter-monomer bond, and we assumed that it occurs instantaneously as soon as the tensile force on the most loaded bond exceeds the bond strength.

η_k (m)	τ_k (s)	ν (m^2 s^{-1})	$\langle\varepsilon\rangle$ (m^2 s^{-3})	$\dot{\gamma}_{eff}$ (s^{-1})	$\Delta t/\tau_k$	Re_λ
54.2×10^{-6}	2.95×10^{-3}	0.996×10^{-6}	0.114	339	0.05	400

TABLE 1. Main parameters of the turbulent flow field simulated by DNS: η_k, Kolmogorov length scale; τ_k, Kolmogorov time scale; ν, kinematic viscosity; $\langle\varepsilon\rangle$, average turbulent dissipation rate; $\dot{\gamma}_{eff}$, effective mean shear rate; Δt, time interval at which each trajectory was sampled by DNS; and Re_λ, Taylor-scale Reynolds number.

2.2. *Direct numerical simulation of the turbulent flow*

For dilute suspensions of small particles, of size much smaller than the Kolmogorov length and having negligible inertia, the geometrical details of the particles can be smoothed out and they can be described as point tracer particles passively carried by the turbulent flow. To this end, we used the results from the DNS of a statistically stationary homogeneous and isotropic three-dimensional turbulent flow, reported as Run II in the papers by Bec *et al.* (2010*a*,*b*). Data are available from the iCFDdatabase (http://cfd.cineca.it). We used the trajectories of 3184 point tracer particles ($St_p = 0$) that were injected at random locations in the simulated turbulent system. The equation of motion for inertialess point particles is

$$\dot{\boldsymbol{X}}(t) = \boldsymbol{u}(\boldsymbol{X}(t), t), \tag{2.7}$$

where $\boldsymbol{u}(\boldsymbol{x}, t)$ is the turbulent velocity field. Each trajectory is sampled at 4720 different times: together with the coordinates $X_i(t)$ of the particle, the components $u_i(\boldsymbol{X}, t)$ of fluid velocity and all the derivatives $\partial u_i/\partial x_j$ of the fluid velocity at the particle positions are available.

The DNS solved the Navier–Stokes equations with large-scale homogeneous and isotropic forcing, on a cubic box with periodic boundary conditions and 2048^3 grid points. Extensive information on the settings and methods used in the simulation is reported in Bec *et al.* (2010*a*,*b*). The simulation assumed a very dilute suspension, where particle–particle interactions and the feedback of particles on the fluid flow were neglected.

The DNS variables are given in arbitrary computational units (see Bec *et al.* 2010*a*, table 1) and were transformed to physical units by prescribing values of ν and η_k that are typical of mechanically stirred aqueous suspensions. The main properties of the turbulent field are listed in table 1.

The analysis of the data along the trajectories made it possible to reconstruct the features of the turbulence that are more relevant to the breakup process and that are shown in figure 1. The probability density functions (p.d.f.s) of ε and $\dot{\gamma}$ are approximately log-normal (Frisch 1995). The log-normal shape of the p.d.f. reflects the fact that the spatial (and temporal) distributions of ε or $\dot{\gamma}$ are characterised by a few sharp peaks of high intensity between regions of low dissipation rate, as visible in figure 2. Although it is customary to describe turbulence in terms of ε, in this work we preferentially use $\dot{\gamma}$, which is linked linearly to the hydrodynamic force acting on the particles.

A practical approach to characterise the local flow type is provided by the so-called mixing index λ_m (Manas-Zloczower & Feke 2009), defined as

$$\lambda_m = \frac{\dot{\gamma}}{\dot{\gamma} + \tilde{\omega}}, \tag{2.8}$$

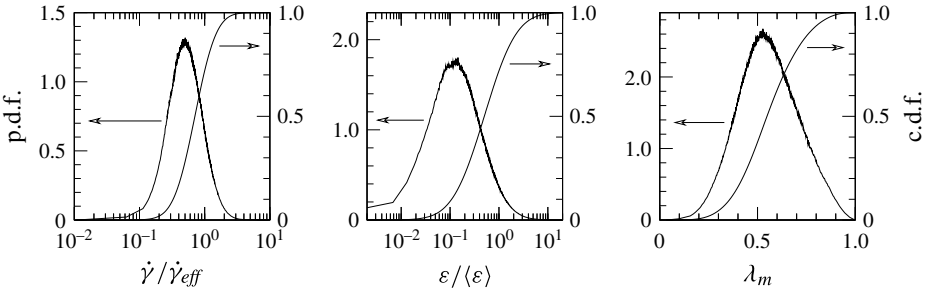

FIGURE 1. Probability density functions (p.d.f. values on the left axes) and cumulative distribution functions (c.d.f. values on the right axes) of shear rate $\dot{\gamma}$, turbulent dissipation rate ε, and mixing index λ_m, in the turbulent flow field.

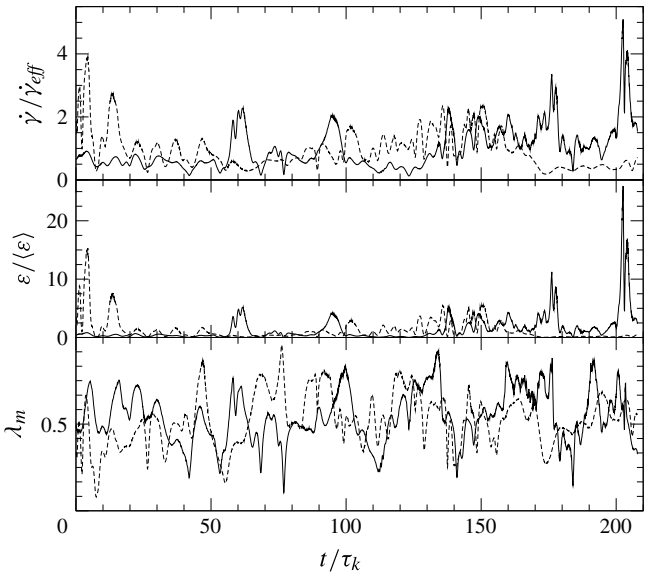

FIGURE 2. Time series of shear rate, turbulence dissipation rate and mixing index along two different particle paths (full and dashed lines).

where $\tilde{\omega}$ is the vorticity of the fluid, which can be evaluated from the antisymmetric component of the velocity gradient:

$$\tilde{\omega} = \sqrt{2\omega_{ij}^{\infty}\omega_{ij}^{\infty}} \quad \text{and} \quad \omega_{ij}^{\infty} = \frac{1}{2}\left(\frac{\partial u_i}{\partial x_j} - \frac{\partial u_j}{\partial x_i}\right). \tag{2.9a,b}$$

The mixing index λ_m has a clear physical interpretation in two-dimensional flows, which can be seen as the superposition of a rotational and an elongational field, and λ_m is the relative weight of the elongational component of the flow. In three-dimensional systems, λ_m does not have such a direct interpretation; nevertheless, it still gives an indication of the elongational character of the flow. In a turbulent flow, the mixing index varies from point to point. The p.d.f. of λ_m is slightly skewed towards the elongational region and, more importantly, shows that the probability of

highly rotational situations in the examined turbulence is very small, whereas that of high elongation is more significant.

2.3. *Stokesian dynamics and internal stresses*

The internal stresses in an aggregate are determined by the interaction of the particle with the local flow field. As observed before, in our case significant variations in the velocity gradient take place on distances much larger than the size of the aggregates. Consequently, in evaluating hydrodynamic stresses, it is reasonable to neglect the curvature of the velocity profiles and assume that the particles are surrounded by a linear flow field with uniform velocity gradient. Under this assumption, Stokesian dynamics (Durlofsky, Brady & Bossis 1987; Brady & Bossis 1988) is an effective tool to determine the hydrodynamic forces and torques acting on the aggregates. The method is valid for conditions of Stokes flow and provides the relationship between the hydrodynamic interactions acting on the particles and their velocity. It is a meshless method, which prescribes implicitly the condition of no slip at particle surfaces and an undisturbed linear flow at infinity, $\boldsymbol{u}^\infty(\boldsymbol{x}) = \boldsymbol{u}^\infty(\boldsymbol{x}_{cm}) + \boldsymbol{\Gamma}^\infty \cdot (\boldsymbol{x} - \boldsymbol{x}_{cm})$, where $\boldsymbol{x}_{cm}$ is the location of the centre of mass of the aggregate. In our approach, the aggregates translate as the point particles of the DNS, and hence the instantaneous value of the velocity gradient $\boldsymbol{\Gamma}^\infty$ in the fluid surrounding the aggregate is provided by the DNS of the flow field.

By using Stokesian dynamics, the hydrodynamic force, torque and stresslet acting on monomer i of an aggregate made of p spherical monomers can be expressed as a linear combination of the linear and rotational velocities of all the monomers relative to the imposed flow and the rate of strain:

$$\begin{bmatrix} m_{11}^{uf} & \cdots & m_{1p}^{uf} & m_{11}^{ul} & \cdots & m_{1p}^{ul} & m_{11}^{us} & \cdots & m_{1p}^{us} \\ \cdots & \cdots & \cdots & \cdots & \cdots & \cdots & \cdots & \cdots & \cdots \\ m_{p1}^{uf} & \cdots & m_{pp}^{uf} & m_{p1}^{ul} & \cdots & m_{pp}^{ul} & m_{p1}^{us} & \cdots & m_{pp}^{us} \\ m_{11}^{\omega f} & \cdots & m_{1p}^{\omega f} & m_{11}^{\omega l} & \cdots & m_{1p}^{\omega l} & m_{11}^{\omega s} & \cdots & m_{1p}^{\omega s} \\ \cdots & \cdots & \cdots & \cdots & \cdots & \cdots & \cdots & \cdots & \cdots \\ m_{p1}^{\omega f} & \cdots & m_{pp}^{\omega f} & m_{p1}^{\omega l} & \cdots & m_{pp}^{\omega l} & m_{p1}^{\omega s} & \cdots & m_{pp}^{\omega s} \\ m_{11}^{ef} & \cdots & m_{1p}^{ef} & m_{11}^{el} & \cdots & m_{1p}^{el} & m_{11}^{es} & \cdots & m_{1p}^{es} \\ \cdots & \cdots & \cdots & \cdots & \cdots & \cdots & \cdots & \cdots & \cdots \\ m_{p1}^{ef} & \cdots & m_{pp}^{ef} & m_{p1}^{el} & \cdots & m_{pp}^{el} & m_{p1}^{es} & \cdots & m_{pp}^{es} \end{bmatrix} \cdot \begin{Bmatrix} \boldsymbol{F}_1 \\ \vdots \\ \boldsymbol{F}_p \\ \boldsymbol{L}_1 \\ \vdots \\ \boldsymbol{L}_p \\ \boldsymbol{S}_1 \\ \vdots \\ \boldsymbol{S}_p \end{Bmatrix}$$
$$= - \begin{Bmatrix} \boldsymbol{u}_1 - \boldsymbol{u}^\infty(\boldsymbol{x}_1) \\ \vdots \\ \boldsymbol{u}_p - \boldsymbol{u}^\infty(\boldsymbol{x}_p) \\ \boldsymbol{\omega}_1 - \boldsymbol{\omega}^\infty(\boldsymbol{x}_1) \\ \vdots \\ \boldsymbol{\omega}_p - \boldsymbol{\omega}^\infty(\boldsymbol{x}_p) \\ -\boldsymbol{e}^\infty(\boldsymbol{x}_1) \\ \vdots \\ -\boldsymbol{e}^\infty(\boldsymbol{x}_p) \end{Bmatrix}. \tag{2.10}$$

In this equation, the entries m_{ij}^{kq}, with $i, j = 1, \ldots, p$ and $k, q = u, \omega, e, f, l, s$, form the so-called mobility matrix, coupling particle velocities to hydrodynamic forces.

Moreover, $\boldsymbol{u}_i$ and $\boldsymbol{\omega}_i$ are the linear and angular velocities of the primary particle i; and $\boldsymbol{F}_i$, $\boldsymbol{L}_i$ and $\boldsymbol{S}_i$ are the hydrodynamic force, torque and stresslet acting on the primary particle. The linear and angular velocities and the deformation rate of the undisturbed flow, $\boldsymbol{u}^\infty$, $\boldsymbol{\omega}^\infty$ and $\boldsymbol{e}^\infty$, must be evaluated at the centre $\boldsymbol{x}_i$ of the monomer. The forces, torques and velocities entering (2.10) are three-component column vectors, while rate-of-strain and stresslet tensors on the right-hand side of the equation are conveniently represented as five-component vectors by taking advantage of the fact that they are symmetric and traceless:

$$\boldsymbol{e}^\infty = \begin{Bmatrix} e^\infty_{xx} - e^\infty_{zz} \\ 2e^\infty_{xy} \\ 2e^\infty_{xz} \\ 2e^\infty_{yz} \\ e^\infty_{yy} - e^\infty_{zz} \end{Bmatrix}, \quad \boldsymbol{S}_i = \begin{Bmatrix} S_{i,xx} \\ S_{i,xy} \\ S_{i,xz} \\ S_{i,yz} \\ S_{i,yy} \end{Bmatrix}. \tag{2.11a,b}$$

In this way, all redundant components are removed from the algebraic system of equations, and the simulation of a cluster of p primary particles leads to an $11p \times 11p$ mobility matrix. This is symmetric, positive definite and depends only on the size and relative position of the monomers and linearly on viscosity (Durlofsky *et al.* 1987).

When Stokesian dynamics is applied to suspensions of freely moving particles, the mobility matrix is normally generated by combining a low-order multipole expansion of the Stokes solution, capable of capturing accurately the hydrodynamic interaction when the particles are relatively far apart, and a correction for near-field interaction, based on lubrication theory. In our approach the latter term was neglected, because lubrication has an effect only on approaching particles, whereas in our rigid clusters all the monomers move at the same velocity, and the addition of the lubrication terms can lead to significant overestimation of the friction force (Bossis, Meunier & Brady 1991). Therefore, we used the far-field form of the mobility matrix, which is obtained by pairwise additivity of the far-field mobility of individual particles. The expressions for the terms of this matrix as functions of the geometric configuration are reported in the literature (Durlofsky *et al.* 1987; Ichiki, Kobryn & Kovalenko 2008). In spite of the approximation involved, the method based on the far-field mobility matrix gives accurate predictions of the motion of rigid clusters, as shown by calculations of the settling velocity of compact aggregates (Harshe, Ehrl & Lattuada 2010, supplementary material) and the rotational velocity of rigid chains of spheres in a shear flow (Vanni & Gastaldi 2011, supplementary material).

The velocity of each primary particle i can be related to the linear and angular velocity of the centre of mass (cm) of the cluster by the condition of rigid-body motion:

$$\begin{cases} \boldsymbol{u}_i = \boldsymbol{u}_{cm} + \boldsymbol{\omega}_{cm} \times (\boldsymbol{x}_i - \boldsymbol{x}_{cm}), \\ \boldsymbol{\omega}_i = \boldsymbol{\omega}_{cm}, \end{cases} \quad i = 1, 2, \ldots, p. \tag{2.12}$$

In addition, in an inertialess aggregate, all forces and torques must be balanced:

$$\begin{cases} \displaystyle\sum_{i=1}^{p} \boldsymbol{F}_i = 0, \\ \displaystyle\sum_{i=1}^{p} [\boldsymbol{L}_i + (\boldsymbol{x}_i - \boldsymbol{x}_{cm}) \times \boldsymbol{F}_i] = 0. \end{cases} \tag{2.13}$$

By substituting (2.12) in (2.10) and adding (2.13) to the resulting system, one finally obtains the following linear system, whose solution gives the forces, torques and stresslets acting on the individual monomers, and the translational and angular velocity of the aggregate:

$$\begin{bmatrix} m_{11}^{uf} & \cdots & m_{1p}^{uf} & m_{11}^{ul} & \cdots & m_{1p}^{ul} & m_{11}^{us} & \cdots & m_{1p}^{us} & \boldsymbol{I} & \boldsymbol{\alpha}_1 \\ \cdots & \cdots & \cdots & \cdots & \cdots & \cdots & \cdots & \cdots & \cdots & \cdots & \cdots \\ m_{p1}^{uf} & \cdots & m_{pp}^{uf} & m_{p1}^{ul} & \cdots & m_{pp}^{ul} & m_{p1}^{us} & \cdots & m_{pp}^{us} & \boldsymbol{I} & \boldsymbol{\alpha}_p \\ m_{11}^{\omega f} & \cdots & m_{1p}^{\omega f} & m_{11}^{\omega l} & \cdots & m_{1p}^{\omega l} & m_{11}^{\omega s} & \cdots & m_{1p}^{\omega s} & \boldsymbol{0} & \boldsymbol{I} \\ \cdots & \cdots & \cdots & \cdots & \cdots & \cdots & \cdots & \cdots & \cdots & \cdots & \cdots \\ m_{p1}^{\omega f} & \cdots & m_{pp}^{\omega f} & m_{p1}^{\omega l} & \cdots & m_{pp}^{\omega l} & m_{p1}^{\omega s} & \cdots & m_{pp}^{\omega s} & \boldsymbol{0} & \boldsymbol{I} \\ m_{11}^{ef} & \cdots & m_{1p}^{ef} & m_{11}^{el} & \cdots & m_{1p}^{el} & m_{11}^{es} & \cdots & m_{1p}^{es} & \boldsymbol{0} & \boldsymbol{0} \\ \cdots & \cdots & \cdots & \cdots & \cdots & \cdots & \cdots & \cdots & \cdots & \cdots & \cdots \\ m_{p1}^{ef} & \cdots & m_{pp}^{ef} & m_{p1}^{el} & \cdots & m_{pp}^{el} & m_{p1}^{es} & \cdots & m_{pp}^{es} & \boldsymbol{0} & \boldsymbol{0} \\ \boldsymbol{I} & \cdots & \boldsymbol{I} & \boldsymbol{0} & \cdots & \boldsymbol{0} & \boldsymbol{0} & \cdots & \boldsymbol{0} & \boldsymbol{0} & \boldsymbol{0} \\ \boldsymbol{\alpha}_1^{\mathrm{T}} & \cdots & \boldsymbol{\alpha}_p^{\mathrm{T}} & \boldsymbol{I} & \cdots & \boldsymbol{I} & \boldsymbol{0} & \cdots & \boldsymbol{0} & \boldsymbol{0} & \boldsymbol{0} \end{bmatrix} \cdot \begin{Bmatrix} \boldsymbol{F}_1 \\ \vdots \\ \boldsymbol{F}_p \\ \boldsymbol{L}_1 \\ \vdots \\ \boldsymbol{L}_p \\ \boldsymbol{S}_1 \\ \vdots \\ \boldsymbol{S}_p \\ \boldsymbol{u}_{cm} \\ \boldsymbol{\omega}_{cm} \end{Bmatrix}$$

$$= \begin{Bmatrix} \boldsymbol{u}^{\infty}(\boldsymbol{x}_1) \\ \vdots \\ \boldsymbol{u}^{\infty}(\boldsymbol{x}_p) \\ \boldsymbol{\omega}^{\infty}(\boldsymbol{x}_1) \\ \vdots \\ \boldsymbol{\omega}^{\infty}(\boldsymbol{x}_p) \\ \boldsymbol{e}^{\infty}(\boldsymbol{x}_1) \\ \vdots \\ \boldsymbol{e}^{\infty}(\boldsymbol{x}_p) \\ \boldsymbol{0} \\ \boldsymbol{0} \end{Bmatrix}. \tag{2.14}$$

In (2.14) $\boldsymbol{0}$ and $\boldsymbol{I}$ are the 3×3 null and identity matrices, respectively, and

$$\boldsymbol{\alpha}_i = \begin{bmatrix} 0 & (z_i - z_{cm}) & -(y_i - y_{cm}) \\ -(z_i - z_{cm}) & 0 & (x_i - x_{cm}) \\ (y_i - y_{cm}) & -(x_i - x_{cm}) & 0 \end{bmatrix}. \tag{2.15}$$

The linear system of equations (2.14) has $11p + 6$ unknowns and its matrix is symmetric but no longer positive definite. It was solved at every time step by using the LAPACK routines dsytrf and dsytrs for factorisation and back-substitution, respectively (Anderson *et al.* 1999). It is convenient to consider the equations in a reference frame moving with the cluster (quasi-Lagrangian frame), because then the matrix does not change with the orientation of the aggregate and thus only a single factorisation is needed.

An isostatic aggregate made by p primary particles shows $p - 1$ inter-particle contacts and the internal stresses at these contacts can be evaluated simply by solving the force and moment balances on each primary particle, without the need to understand in detail the nature of the inter-monomer interaction (Gastaldi & Vanni 2011; Seto *et al.* 2011). For the ith monomer of the aggregate, these balances read

as follows:

$$\boldsymbol{F}_i + \sum_{j=1}^{p} \beta_{j,i} \boldsymbol{f}_{j,i} = 0, \quad i = 1, \ldots, p, \tag{2.16}$$

$$\boldsymbol{L}_i + \sum_{j=1}^{p} \beta_{j,i} \left[\boldsymbol{l}_{j,i} + \frac{\boldsymbol{x}_j - \boldsymbol{x}_i}{2} \times \boldsymbol{f}_{j,i} \right] = 0, \quad i = 1, \ldots, p, \tag{2.17}$$

where $\boldsymbol{f}_{j,i}$ and $\boldsymbol{l}_{j,i}$ are the internal force and torque acting on monomer i at the contact with monomer j, and $\beta_{j,i}$ is a variable that is set equal to unity if monomers i and j are in contact and zero otherwise. Only $6(p-1)$ out of the $6p$ equations above are independent, because the balance of force and moment for the whole aggregate given by (2.13) prescribes that the sums of all internal forces and of all internal moments must vanish. Therefore, the solution of the linear system obtained by taking the equations above for the first $p-1$ particles gives all the required components of the internal forces and torques acting on the $p-1$ internal bonds. The force acting at each contact is then decomposed into a normal component N, acting on the line joining the centres of the monomers, and a tangential component T, acting in the perpendicular direction. Similarly, the torque is decomposed into a twisting moment M_t, which generates the spinning deformation around the centre–centre axis, and a bending moment M_b, which induces mutual rolling of the two monomers.

The translational and rotational aggregate velocities should be obtained by solving the system of equations (2.14), which require knowledge of the gradient velocity tensor fields. Here we make the hypothesis that the centre of mass translates with the flow velocity at its position:

$$\boldsymbol{u}_{cm}(t) = \boldsymbol{u}(\boldsymbol{x}_{cm}(t), t). \tag{2.18}$$

This assumption does not give rise to any error if the particle is axisymmetric, as in the case of doublets, but is not fully correct in the case of disordered aggregates, whose velocity may be different from that of fluid particles. However, the error is minor and does not invalidate the results. For example, with the clusters of 384 primary particles studied in § 4, the estimated error in particle position is always less than $d/10$ (d being the outer diameter of the aggregate). As we assumed $d \ll \eta_k$, such a displacement is much smaller than the Kolmogorov length scale, and consequently the cluster is always located in a region where the velocity gradient does not deviate significantly from the value of the DNS trajectory. Hence, the translational motion of the aggregate was provided by the DNS. Differently, the rotation around its centre of mass was calculated by integration of the angular velocity $\boldsymbol{\omega}_{cm}$ obtained by (2.14) by an explicit Euler method with a time step 10 times smaller than the sampling time of DNS trajectories. At every time step, the angular motion consisted of a rotation of the angle $\Delta\varphi = |\boldsymbol{\omega}_{cm}(t)|\Delta t$ around the unit vector $\boldsymbol{n} = \boldsymbol{\omega}_{cm}/|\boldsymbol{\omega}_{cm}|$. The new coordinates of the monomers after the operation are given by the following equation (Goldstein, Poole & Safko 1983):

$$\boldsymbol{x}_i(t + \Delta t) = \boldsymbol{x}_{cm}(t + \Delta t) + \boldsymbol{R} \cdot (\boldsymbol{x}_i(t) - \boldsymbol{x}_{cm}(t)), \tag{2.19}$$

where the rotation matrix is

$$\boldsymbol{R} = \begin{bmatrix} \cos\Delta\varphi + n_x^2(1-\cos\Delta\varphi) & n_x n_y(1-\cos\Delta\varphi) - n_z \sin\Delta\varphi & n_x n_z(1-\cos\Delta\varphi) + n_y \sin\Delta\varphi \\ n_y n_x(1-\cos\Delta\varphi) + n_z \sin\Delta\varphi & \cos\Delta\varphi + n_y^2(1-\cos\Delta\varphi) & n_y n_z(1-\cos\Delta\varphi) - n_x \sin\Delta\varphi \\ n_z n_x(1-\cos\Delta\varphi) - n_y \sin\Delta\varphi & n_z n_y(1-\cos\Delta\varphi) + n_x \sin\Delta\varphi & \cos\Delta\varphi + n_z^2(1-\cos\Delta\varphi) \end{bmatrix}. \tag{2.20}$$

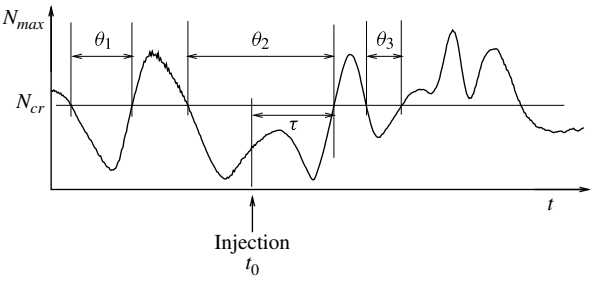

FIGURE 3. Schematic of the time series of the instantaneous maximum normal stress N_{max} acting on an aggregate that moves in the turbulent flow field. If the aggregate were injected in the field at time t_0, its breakage time would be τ. The diving times θ_1, θ_2 and θ_3 for a given stress threshold N_{cr} are also shown.

2.4. *Breakup frequency*

Since the studied aggregates are not statically overconstrained, their breakage is originated by the failure of a single bond and the subsequent separation of the two contacting monomers, giving two fragments. The failure occurs whenever the normal force acting on the bond is tensile and exceeds the critical pull-off value given by contact mechanics (Johnson 1985):

$$N_{cr} = \kappa \pi a \sigma, \tag{2.21}$$

where σ is the surface energy of the contact, a is the radius of the contacting primary particles, and κ is a parameter that ranges between 1.5 and 2.0 depending on the physical properties of the contact (Maugis 1992; Carpick, Ogletree & Salmeron 1999). As reviewed by Bäbler *et al.* (2008), a number of experimental and theoretical works suggest that rigid aggregates are brittle and hence breakup occurs almost instantaneously as soon as the pull-off force is exceeded.

In this work we apply first-passage-time statistics (Redner 2001) to estimate the breakup frequency from the distribution of the time necessary for observing the first occurrence of a normal stress strong enough to sever a bond and, consequently, break the aggregate. Considering an aggregate injected in the flow field at random space and time coordinates, its breakup time τ is the time needed for it to reach the condition $N > N_{cr}$ on any of its bonds for the first time (provided that at injection time $N < N_{cr}$). The breakup frequency for a class of aggregates is the inverse of the mean breakup time, obtained by averaging τ over many different injections and aggregate realisations (Bäbler *et al.* 2012):

$$f_{br} = \frac{1}{\langle \tau \rangle}. \tag{2.22}$$

The mean breakup time can be obtained by the analysis of the time series of the largest instantaneous normal stress acting on each aggregate, N_{max}. An example of such a time series is plotted in figure 3. Given the pull-off threshold N_{cr} for the normal stress, one can measure the sequence of *diving times* $\theta_1, \theta_2, \theta_3, \ldots$, that is, the lengths of the intervals of time in which N_{max} is below the threshold N_{cr} and breakup does not happen. The moments of the distribution of diving times for all aggregates can be

related to the mean breakage time as follows (Bäbler *et al.* 2012):

$$\langle \tau \rangle = \frac{\langle \theta^2(N_{cr}) \rangle}{2\langle \theta(N_{cr}) \rangle}. \tag{2.23}$$

Finally, by sampling the size of the two fragments that are formed each time an aggregate is broken (that is, whenever N_{max} becomes greater than N_{cr}), one can estimate the fragment distribution function of the process.

The approach is similar to the one adopted recently by Bäbler *et al.* (2012). In that case, however, it was assumed that breakup occurred whenever a critical value of dissipation rate was overcome and the role of internal stresses was not taken into account. Here, instead, breakup is determined by the combined effect of the dissipation rate and the orientation of the aggregate, which determine the internal stress. As shown below, the interaction between the two effects can be relevant and should be taken into account. In addition, by considering the structure of the aggregate, it is possible to identify the failed contact and to extract statistics on the fragment size distribution.

The non-normal interactions are not capable of breaking the aggregate but may lead to its restructuring. This process may proceed through mutual sliding of the contacting monomers induced by transverse forces, relative twisting by torsional moments or mutual rolling due to bending moments. For aggregates made of spherical monomers, the most relevant restructuring mechanism is mutual rolling, which is determined by a critical value in the bending moment (Vanni & Gastaldi 2011). However, the theory to determine the onset of rolling is not so well established as the method to predict particle detachment. Therefore, although in this paper we give indications on the magnitude and the distribution of the bending moment, the process of restructuring is not examined in detail.

3. A simple configuration: the doublet

As a first step, we investigated the response of a rigid doublet of equal-sized and contacting spheres to turbulence. In the study of breakup, the doublet has been used several times as the prototype of aggregates that break into two fragments because of the presence of a weak region in between (Tadmor 1976; Dukhin *et al.* 2005; Calvert, Ghadiri & Tweedie 2009; Manas-Zloczower & Feke 2009). Furthermore, the problem of the motion of a doublet in linear velocity fields has an exact analytical solution and thus allows validation of our method based on Stokesian dynamics.

3.1. *Validation of the method*

The rotational motion of an axisymmetric body in a three-dimensional linear flow field at creeping flow conditions obeys the following equation (Guazzelli & Morris 2012, p. 75):

$$\frac{\mathrm{d}\boldsymbol{p}}{\mathrm{d}t} = \boldsymbol{\omega}^{\infty} \times \boldsymbol{p} + \beta[\boldsymbol{e}^{\infty} \cdot \boldsymbol{p} - \boldsymbol{p}(\boldsymbol{p} \cdot \boldsymbol{e}^{\infty} \cdot \boldsymbol{p})], \tag{3.1}$$

where the director $\boldsymbol{p}$ is the unit vector in the direction of the symmetry axis and the Bretherton constant (Bretherton 1962) for a doublet made of equal-sized and contacting spheres is $\beta = 0.5942$.

When applied to a doublet positioned on the x–y plane and immersed in a simple shear flow with prescribed velocity gradient $\dot{\gamma} = \mathrm{d}u_x^{\infty}/\mathrm{d}y$, the previous equation gives

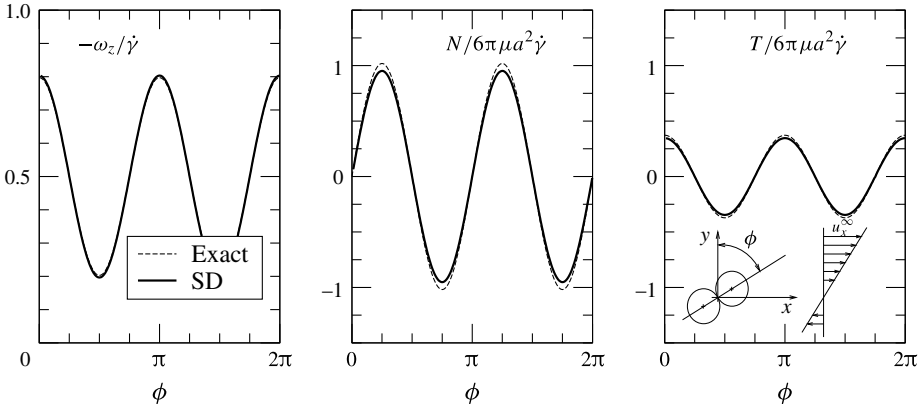

FIGURE 4. Angular velocity and hydrodynamic forces for a doublet versus orientation: dashed line, exact solutions, (3.2), (3.3) and (3.4); full line, Stokesian dynamics.

the following expressions for the angular velocity of the body:

$$\omega_x = \omega_y = 0, \quad \omega_z = -\tfrac{1}{2}\dot{\gamma}[1 + \beta\cos(2\phi)], \tag{3.2a,b}$$

where the angle ϕ defines the orientation of the doublet in the plane x–y in a fixed frame of reference.

The internal bending and twisting moments acting at the contact region of the two monomers, owing to symmetry, are always nil for a freely suspended doublet. Instead, the normal and tangential components of the hydrodynamic force acting on either sphere of the doublet are given by the following expressions, obtained by applying the solution for a general linear flow by Nir & Acrivos (1973) to our configuration:

$$N = \pi\mu\frac{a^2}{2}\dot{\gamma}(h_1 + h_2)\sin(2\phi), \tag{3.3}$$

$$T = \pi\mu\frac{a^2}{2}\dot{\gamma}h_1\cos(2\phi), \tag{3.4}$$

where $h_1 = 4.463$ and $h_2 = 7.767$. Therefore the doublet simply rotates in the x–y plane and alternates intervals of traction and compression. As the doublet is rigid, the two monomers always remain in contact and cannot move apart during traction.

As apparent from figure 4, the Stokesian dynamics data agree well with the exact solution for the rotational velocity of the doublet, with an error around 1 %. The estimated dimensionless doublet rotation period is $t_r\dot{\gamma} = 15.8$, against the theoretical value $t_r\dot{\gamma} = 2\pi(q + 1/q) = 15.6$. The variable q is the eccentricity of the ellipsoid that moves with the same angular velocity as our doublet and is related to the Bretherton constant by $\beta = (q^2 - 1)/(q^2 + 1)$. Concerning the internal forces N and T, the difference between Stokesian dynamics and the exact solution is larger (approximately 6 %), but still fairly good.

For any given linear flow field, the instantaneous values of angular velocity and internal forces depend only on the orientation of the doublet with respect to the velocity gradient. As a consequence, it is important to characterise the error in the orientation and its accumulation in time during the motion of the particle in the turbulent flow. This is why we compared the orientation of the doublet given by the

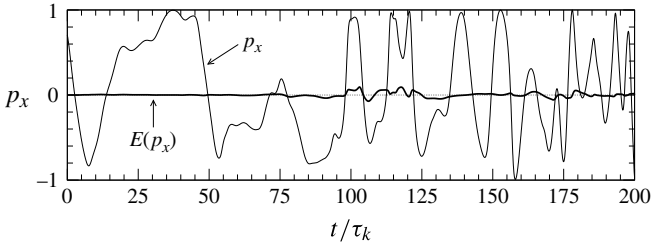

FIGURE 5. The x component of the director vector of the doublet, p_x, for one turbulent trajectory calculated by accurate solution of (3.1) and absolute error of the Stokesian dynamics simulation, $E(p_x)$.

Stokesian dynamics method with the result of an accurate integration of the ordinary differential equation (3.1) for some of the particle paths provided by the DNS. A result showing the behaviour of the x component of the director vector is reported in figure 5. The error of Stokesian dynamics with respect to the accurate integration is always below 4–5 %, even in the presence of sudden changes of orientation. The component of such error due to the numerical discretisation is almost negligible (approximately 3 % of the total error), as verified by integrating the equations with much smaller time steps. In addition, no significant degradation of the rotation matrix $\boldsymbol{R}$ was found at the end of the integration. Hence, the error is essentially generated by the approximate mobility matrix, which is estimated from a multipole expansion of the solution of the Stokes equations truncated to first order. As observed before for a doublet aligned in the shear plane, Stokesian dynamics gives errors around 1 % in the prediction of the angular velocity. However, the rotation of the particle and the fluctuating flow field act in such a way as to balance the error and avoid its increase as the simulation time becomes larger.

3.2. *Stress distribution and breakup rate*

As shown by the plot of angular velocity in figure 6, a doublet rotates irregularly in the turbulent field and hence changes its orientation continuously with respect to the velocity gradient. As a consequence, the normal stress N alternates conditions of traction and compression, changing in sign at intervals that are on average around $5\tau_k$. The transverse force T also oscillates, and changes direction alternately, although this last feature cannot be seen in the figure, where only the modulus of T is plotted. The peaks of T normally occur when the angular velocity is large and have smaller intensity in comparison to the peaks of N.

The angular velocity ω of a doublet is determined above all by the shear rate $\dot{\gamma}$ of the flow field, and indeed the probability distribution for ω is log-normal as for the shear rate (figure 7). The p.d.f. of the normal stress includes both positive and negative components and is described quite well by an exponential law decaying as $\mathrm{e}^{-\alpha|x-\bar{x}|}$ or, for large values of x, as $\mathrm{e}^{-\alpha x}$. As also observed by Derksen (2008), tensile stresses prevail over compressive ones, and the probability that normal stresses are compressive, i.e. negative, is only 31 %, as shown by the cumulative density function. This fact is not an inhomogeneous sampling of the flow by the aggregate, since in our work particle inertia is neglected. Rather, it may be a consequence of the preferential alignment with vorticity shown by elongated particles in turbulent flows (Pumir & Wilkinson 2011; Parsa *et al.* 2012). The skewness of the distribution towards positive

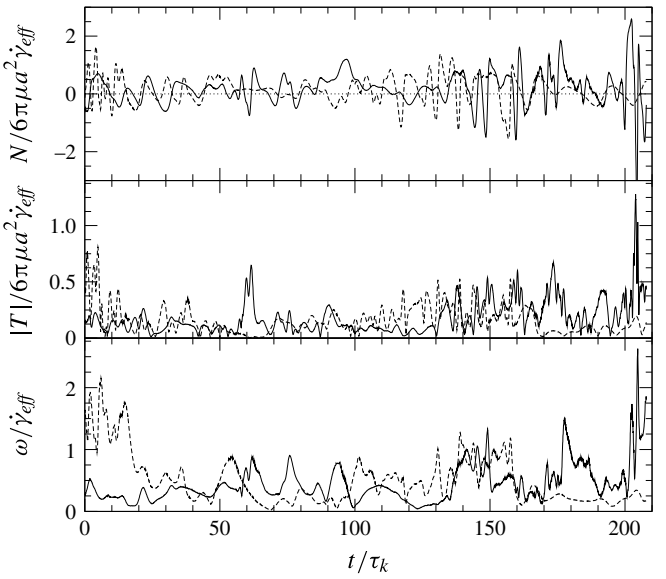

FIGURE 6. Time series of normal force N, transverse force T and angular velocity ω for a doublet along two different paths (full and dashed lines; same paths as in figure 2).

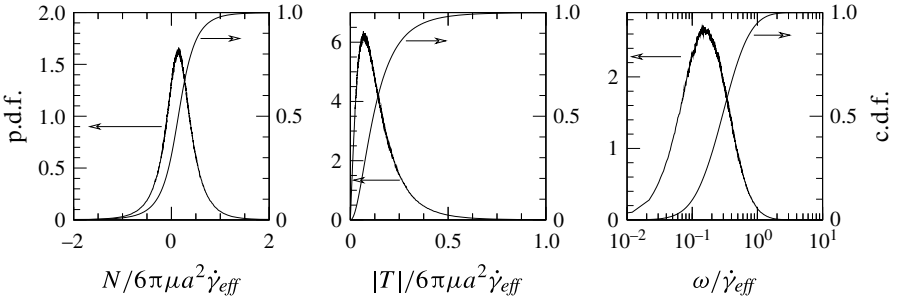

FIGURE 7. Probability density functions (p.d.f. values on the left axes) and cumulative distribution functions (c.d.f. values on the right axes) of the inter-monomer normal force N, transverse force T and the angular velocity ω of doublets in the turbulent flow field.

normal stresses is also apparent in the joint shear rate–normal stress distribution of figure 8. The density function is enclosed by the two theoretical limits of largest tensile and compressive stresses, which are $|N|/(6\pi\mu a^2\dot{\gamma}_{eff}) \leqslant [(h_1 + h_2)/12](\dot{\gamma}/\dot{\gamma}_{eff})$, according to the solution by Nir & Acrivos (1973). It is worth observing that, since $(h_1 + h_2)/12 = 1.019 \approx 1$, the term $(6\pi\mu a^2\dot{\gamma})$ is a good approximation of the largest tensile force that should be expected on a doublet immersed in a flow field of strength $\dot{\gamma}$.

The breakup frequency was estimated by applying the first-passage-time analysis described in § 2.4 on the full set of the time series of the normal stress and is plotted in figure 9. It was evaluated for different values of the variable $\mathscr{N} = N_{cr}/(6\pi\mu a^2\dot{\gamma}_{eff})$ or $\mathscr{E} = 1/\mathscr{N}^2 = (6/\kappa)^2(\varrho a/\sigma)^2\nu\langle\varepsilon\rangle$, where N_{cr} is related to surface energy by (2.21) and $\dot{\gamma}_{eff}$ to $\langle\varepsilon\rangle$ by (1.2). The numerator of $\mathscr{N}$, N_{cr}, is the cohesive strength of the bond, whereas the denominator, as observed before, estimates the largest tensile stress acting

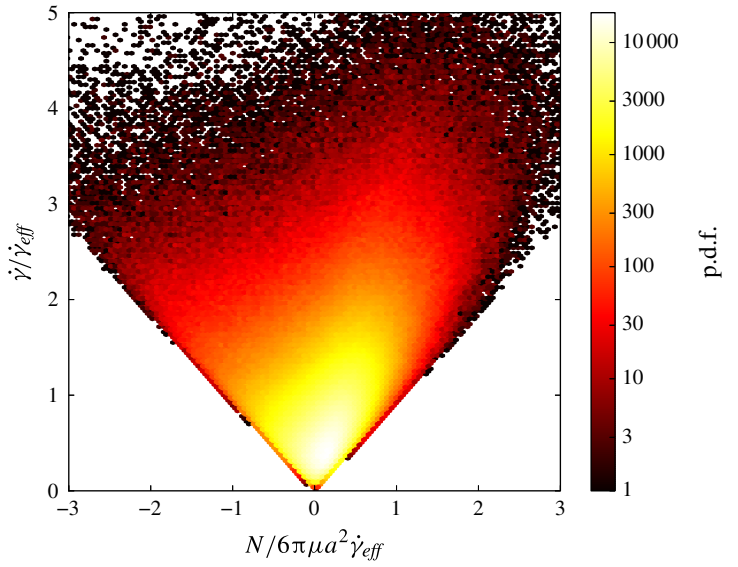

FIGURE 8. (Colour online) Joint shear rate–normal stress distribution for doublets in the turbulent flow. Note that the scale of the density function is logarithmic in order to better capture the region where the p.d.f. is very small.

on the bond at the effective shear rate $\dot{\gamma}_{eff}$. As it is the ratio of these two variables that determines $\mathscr{N}$ and governs breakup, the same effect can be achieved by acting on either of these variables. Hence, low values of $\mathscr{N}$ are obtained with weak bonds or, equivalently, strong turbulence. The breakup frequency decreases monotonically with $\mathscr{N}$ and, conversely, increases with $\mathscr{E}$. Two asymptotic regimes (slow and fast breakup) can be observed with exponential dependence between frequency and $\mathscr{E}^{-1/2}$:

$$f_{br} \propto \sqrt{\frac{\langle\varepsilon\rangle}{\nu}}\exp\left(-\frac{\alpha}{\sqrt{\mathscr{E}}}\right). \tag{3.5}$$

For a given cohesive force, the slow breakage regime takes place in the systems with weaker turbulence ($\mathscr{N} > 1.5$ or $\mathscr{E} < 0.5$). In this case, by fitting the data, we obtain $\alpha = 1.8$. For $\mathscr{N} < 0.5$ or $\mathscr{E} > 5$ we are in the fast breakage situation, where the fitted constant is now $\alpha = 4.8$.

For the slow breakup region, the exponential dependence of (3.5) can be justified considering that the breakup rate is equal to the frequency at which the normal force N exceeds the pull-off value N_{cr}. The normal force is generated by the turbulent fluctuations, whose frequency is of the order of $1/\tau_k$. However, only the fluctuations for which N crosses the value N_{cr} are effective for breakup. Overall, the probability of attaining such a condition is proportional to the p.d.f. of the normal stress evaluated in N_{cr}, which is a function that decays exponentially with $\mathscr{N}$. If the statistics of the normal stress are preserved within single fluctuations, then the expected breakup frequency becomes indeed $f_{br} \propto (1/\tau_k)\,\mathrm{e}^{-\alpha\mathscr{N}} = \sqrt{\langle\varepsilon\rangle/\nu}\;\mathrm{e}^{-\alpha/\sqrt{\mathscr{E}}}$.

4. Stress distribution in cluster–cluster aggregates

Aggregates were generated numerically by using a tunable CC method, capable of producing aggregates made of spherical primary particles of radius a and prescribed

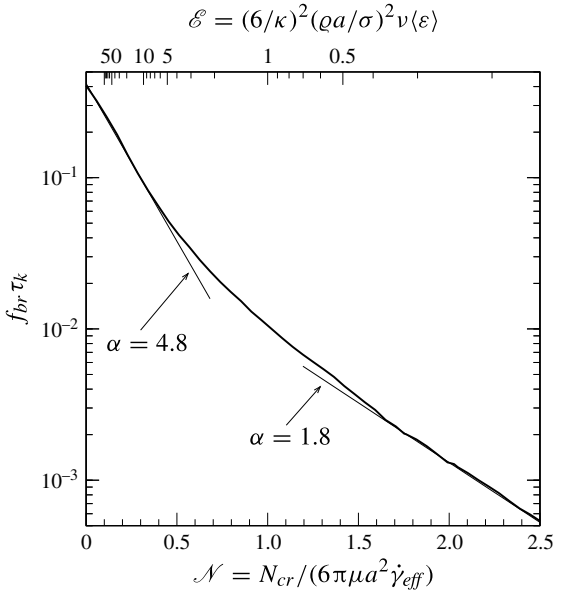

FIGURE 9. Breakup frequency of a doublet as a function of critical stress and average turbulence dissipation rate. The two asymptotic regimes of fast and slow breakup are shown by the straight lines.

fractal dimension D_f (Thouy & Jullien 1994; Filippov, Zurita & Rosner 2000). According to the fractal scaling law, the total number of primary particles p in an element of the population of aggregates is related to its gyration radius R_g by the following equation:

$$p = k_f \left(\frac{R_g}{a}\right)^{D_f}. \tag{4.1}$$

For our particles, the fractal law was satisfied exactly at each step of the hierarchical generation method (i.e. at the level of trimers, hexamers, 12-mers, etc.). The presence of a fractal structure in the generated aggregates was also checked by examination of the slope of the two-point density–density correlation function, which counts the average number of primary particles at a distance r from any primary particle in the cluster (Sorensen & Roberts 1997). Most of the following results concern aggregates made of 384 primary particles with $D_f = 1.9$, $k_f = 1.2$ and $R_g/a = 20.8$.

The upper part of figure 10 shows the forces acting on the monomers of an aggregate immersed in the turbulent flow field at a certain time. The forces act in different directions as a consequence of the three-dimensional instantaneous flow field. They are more intense on the external monomers, owing to the larger slip velocity and the smaller hydrodynamic shielding. The centre of mass of the aggregate moves with the same velocity as the undisturbed flow, and hence the slip velocity between primary particles and fluid is larger for the outer monomers owing to the velocity gradient. In addition, when reaching the most exposed external monomers, the fluid flow is not hindered or screened by the presence of other particles along its path, and the drag force is not significantly reduced with respect to the case of free draining.

External forces generate a stress state in the branches of the aggregate: the lower part of figure 10 reports the normal component of the inter-monomer interaction under

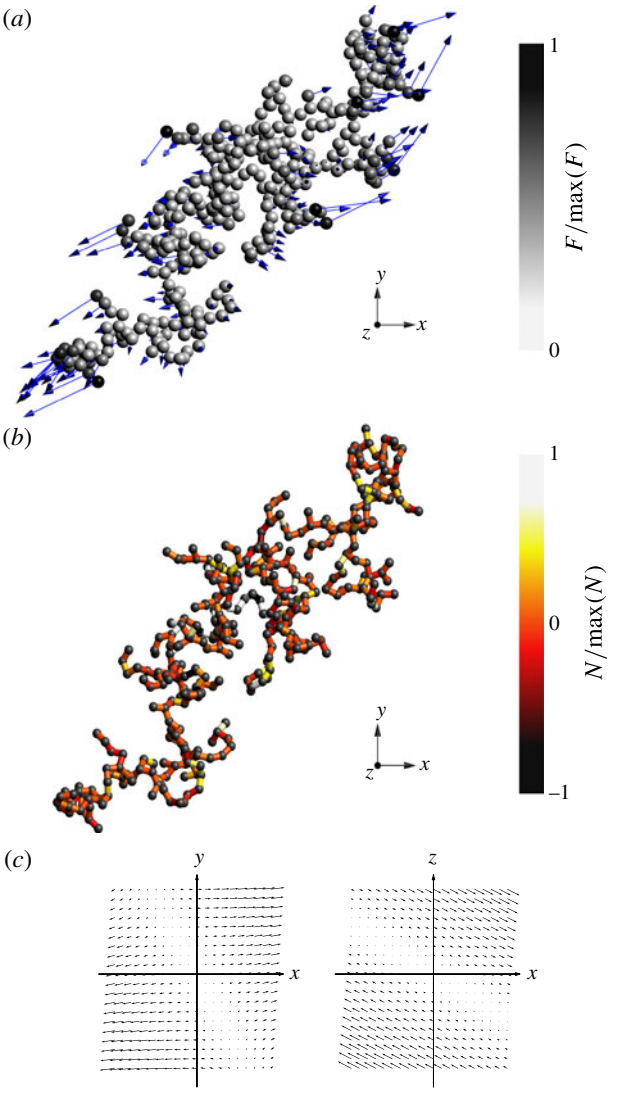

FIGURE 10. (Colour online) (*a*) Instantaneous hydrodynamic forces and (*b*) internal normal forces for a CC aggregate made of 384 primary particles with $D_f = 1.9$ and $k_f = 1.2$. (*c*) The instantaneous flow field $\boldsymbol{u}^\infty$ in the x–y and x–z planes shown by vector plots.

the same conditions. Internal forces operate at inter-monomer bonds, which have been shown by drawing them as small rods whose colour reflects the intensity of the normal force. The most stressed bonds, which correspond to the highest values of tensile normal force, can be identified by the white colour. As already observed in previous papers (Gastaldi & Vanni 2011; Vanni & Gastaldi 2011), these critical bonds are located in the inner region of the cluster and may be quite far from the monomers with the highest external loads. This is consequence of the structure of low-density aggregates, which are made mostly of chains of primary particles along which the stress generated by the external forces is propagated and accumulated.

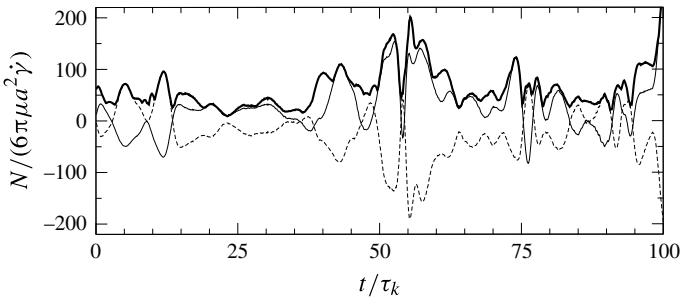

FIGURE 11. Fluctuating normal force (thin lines) at two inter-monomer contacts for the aggregate of figure 10, and maximum value of N (thick line) over all the bonds of the aggregate, N_{max}.

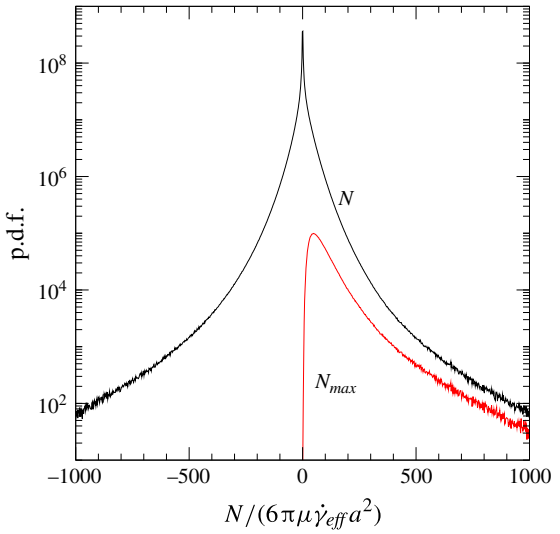

FIGURE 12. (Colour online) Probability density functions for N and N_{max} for aggregates with $p = 384$, $D_f = 1.9$ and $k_f = 1.2$ in the turbulent flow field. Data are from a family of 30 different clusters on 3184 trajectories and sampled at 1393 different times. The area below each curve is equal to the number of samples used to build the p.d.f.

Aggregates move and rotate in the turbulent flow field and hence each inter-monomer contact feels a fluctuating force that alternates between traction and compression. This behaviour is shown in figure 11, where the normal force component at two bonds of the aggregate of figure 10 is plotted along time. The figure also reports N_{max}, that is, the largest value of N over all the inter-monomer bonds of the cluster at a given time. Since our aggregates are isostatic, breakup takes place whenever the tensile stress exceeds the pull-off value at the most loaded contact of the aggregate. Therefore, it is N_{max} that should be compared with the threshold value for pull-off in order to determine the occurrence of breakup.

As shown in figure 12, the probability distribution of the normal inter-monomer force follows approximately a stretched exponential function, $\mathrm{e}^{-|kx|^q}$, with $q \approx 1/3$. The figure includes the data from all the bonds of a family of 30 different aggregates with the same morphology (i.e. the same values of p, D_f and k_f) on the 3184

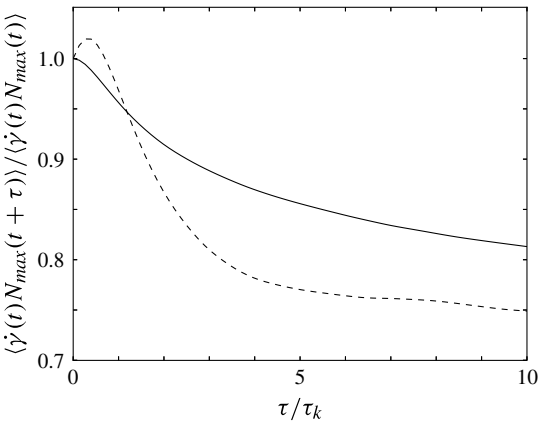

FIGURE 13. Correlation between instantaneous shear rate and maximum stress for doublets (dashed line) and the population of CC aggregates (full line).

turbulent trajectories. As every bond alternates between traction and compression, the distribution shows positive and negative values of N. Differently from the doublet, where traction prevails, in this case the distribution is symmetrical and centred at $N = 0$. The reason for the different behaviour lies in the random orientation of the bonds. While at the level of a single contact the distribution may be biased towards compression (for example, the thin dashed line of figure 11) or traction (the thin full line), when all the bonds of the family of clusters are taken into account, this effect vanishes and the distribution is balanced and symmetrical.

When only the maximum normal force N_{max} is considered, the situation changes substantially. For these aggregates, a time series of N_{max}, such as the one shown by the thick line of figure 11, always mirrors the time series of $\dot{\gamma}$. At any time, for these large aggregates, there exists at least one bond where the effect of the strain rate is enhanced, owing to favourable location and orientation, and, consequently, a peak in $\dot{\gamma}$ always implies a simultaneous peak in N_{max}. As a consequence, the p.d.f. of N_{max}, too, reflects that of $\dot{\gamma}$, and in fact exhibits a similar shape, as apparent by comparing the distributions shown in figures 1 and 14. Again, this situation is different from that of a doublet, where there is smaller correlation between the instantaneous values of N_{max} ($= N$ in this case) and $\dot{\gamma}$, because the orientation of the single bond of the doublet is not always favourable to the generation of a tensile state of stress. This fact is shown more quantitatively in figure 13, where the correlation $\langle \dot{\gamma}(t) N_{max}(t+\tau) \rangle$ is plotted for the doublet and the population of CC aggregates. While for large aggregates the maximum of correlation occurs at the initial time, the doublet shows a certain delay in reaching the proper alignment with the flow field, which is reflected by a shift in the location of the maximum. In addition, the correlation is narrower and decays significantly faster than for CC aggregates.

The restructuring of aggregates made of spherical monomers is normally determined by the bending moment M and, in particular, by the distribution of M_{max}, the largest value of M over all the bonds of the aggregate. The behaviour of M_{max} and N_{max} is very similar, as visible in figure 14, and both reproduce that of the shear rate.

Figure 14 also plots the statistical distribution of the radial location at which the maximum stress (either N_{max} or M_{max}) occurs, i.e. the region where rupture or restructuring are more likely to initiate. Owing to the complex shape of the clusters,

	Average	Std dev.
$N_{max}/6\pi\mu R_g^2\dot{\gamma}_{eff}$	0.231	0.217
$M_{max}/6\pi\mu R_g^3\dot{\gamma}_{eff}$	0.117	0.088
$r(N_{max})/R_g$	0.712	0.288
$r(M_{max})/R_g$	0.769	0.230

TABLE 2. Average and standard deviation of the stress distributions for the population of aggregates with $p = 384$, $D_f = 1.9$ and $k_f = 1.2$.

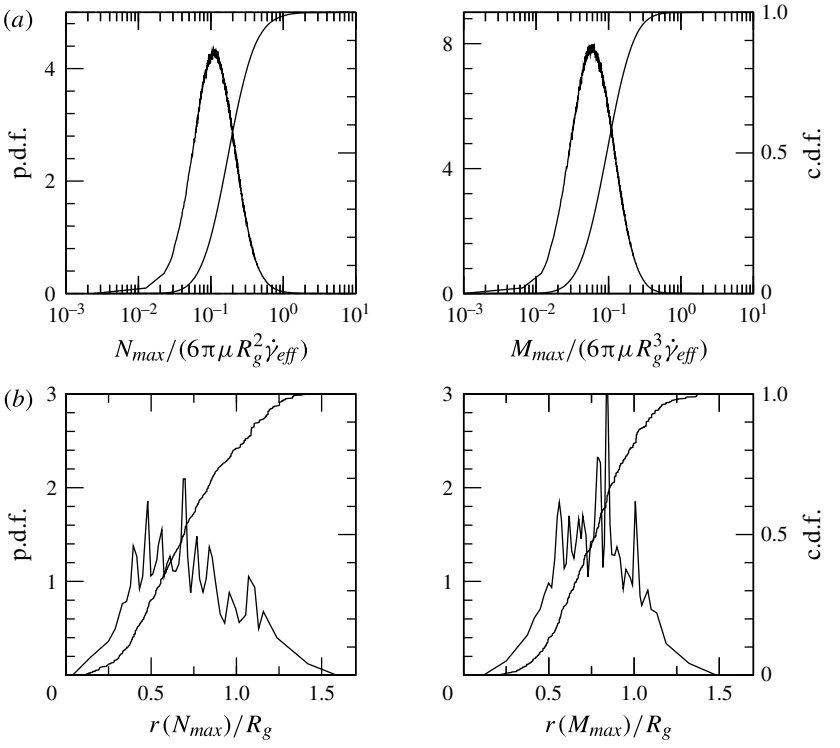

FIGURE 14. Statistical distributions for the population of aggregates with $p = 384$, $D_f = 1.9$ and $k_f = 1.2$: (*a*) maximum normal force and bending moment; (*b*) radial location of N_{max} and M_{max} with respect to the aggregate centre of mass.

the spatial region around the centre of mass is often empty, and the most stressed contacts, generated by the mechanism of accumulation of internal forces along filaments, are normally located in a region that is approximately midway between the centre of mass and the periphery of the aggregate. For the normal force, the highest stress is usually in the interval $0.4 < r/R_g < 0.9$; the most intense bending moments, which have a narrower distribution, are located in $0.5 < r/R_g < 0.8$. Table 2 reports average values and standard deviations for all these distributions, based on the population of clusters made by 384 primary particles. Data are scaled by the radius of gyration because, as shown below, this is the relevant length scale for aggregate stress statistics.

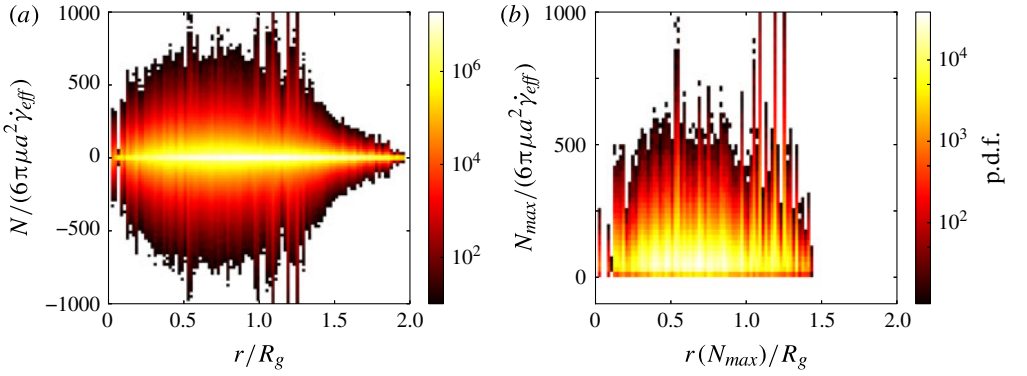

FIGURE 15. (Colour online) (*a*) Joint p.d.f. between normal force and location. (*b*) Joint p.d.f. between maximum instantaneous force and location. Aggregates with $p = 384$, $D_f = 1.9$ and $k_f = 1.2$; data are from the simulation of 3184 trajectories with 30 different aggregate realisations. The scale of the density function is logarithmic to better describe the region of low p.d.f.

The joint distribution of contact force N and contact location r is shown in the left graph of figure 15. It further confirms that traction and compression are equally probable and the distribution is symmetric with respect to $N = 0$. The strength of N on most bonds is very small, while the occurrence of large values of normal force, in either compression or traction, is quite uncommon. Surprisingly, even when the distribution of N_{max} is considered, most conditions still correspond to very small values of the normal force, while high values of N_{max} occur only at few favourable locations and at particular times. By comparing the distributions of N and N_{max}, one can observe that, within the collected statistics, the instantaneous maximum of N never occurs in the outer shell of the aggregate ($1.5 < r/R_g < 2.0$).

A previous analysis for pure shear flow suggested that the proper scaling length for the maximum instantaneous internal forces was the radius of gyration (Vanni & Gastaldi 2011). In that case, by scaling the radial coordinate r by R_g, N_{max} by R_g^2 and M_{max} by R_g^3, the stress distributions, at least approximately, collapsed onto a single curve, which was independent of particle size, number of monomers and fractal dimension. This feature is retained by the turbulent flow, owing to the linearity of the flow field at the scale of the aggregates. Figure 16 shows that the statistical distributions of N_{max} obtained in the studied isotropic turbulence by aggregates with a number of monomers ranging from 192 to 768 lie on a single curve when scaled by R_g^2. The proportionality by N_{max} and R_g^2 can be explained by considering that the maximum internal stress originates from the accumulation of drag forces along the chains of monomers that are most exposed to the flow field. The drag force on the monomers of such almost unshielded filaments is roughly proportional to r, because of the linear flow surrounding the aggregate, while the length of the chains is comparable to the radius of gyration. The moment scales with R_g^3 because of the additional role of the arm of the force. This explanation is confirmed by the fact that in uniform flows, where the drag force on the monomers of the unscreened filaments is approximately constant, N_{max} and M_{max} become proportional to R_g and R_g^2, respectively (Gastaldi & Vanni 2011). It is worth noting that such a scaling is not valid in general for N, M or their average values. The accumulation effect that determines N_{max} and M_{max} occurs only on the branches with a favourable (elongated

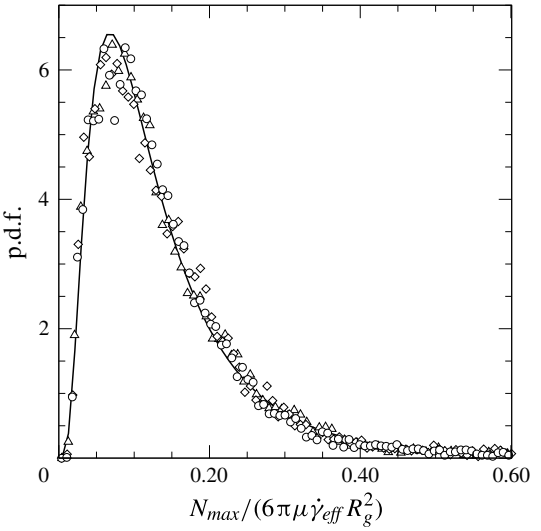

FIGURE 16. Statistical distribution of N_{max} for aggregates with $D_f = 1.7$: circles, 768 primary particles ($R_g = 42.7$); diamonds, 384 primary particles ($R_g = 28.4$); triangles, 192 primary particles ($R_g = 18.9$). For each condition, we examined the response of 10 different clusters on 633 trajectories.

and unshielded) spatial configuration, whereas for short, wrapped or hydrodynamically screened branches the effect is negligible.

The breakup frequency was estimated by applying first-passage-time analysis on the time series of the maximum internal normal force N_{max}. The mean breakup time $\langle\tau\rangle$ was evaluated by the sequence of diving times obtained by comparing the profile of N_{max} with the pull-off value N_{cr} for the full set of 3184 trajectories and 30 realisations of aggregates with $p = 384$, $k_f = 1.2$, $D_f = 1.9$ and $R_g/a = 20.8$. However, the results can be extended to different situations by taking advantage of the scaling properties of N_{max} with R_g^2, and indeed figure 17 plots the dimensionless breakup frequency as a function of $\mathscr{N} = N_{cr}/(6\pi\mu\dot{\gamma}_{eff}R_g^2)$. Obviously, the scaling is valid only for the conditions in which it was tested, that is, low-density isostatic CC aggregates ($1.7 \leqslant D_f \leqslant 2.3$). As turbulence is normally characterised in terms of the mean dissipation rate $\langle\varepsilon\rangle$ and adhesion in terms of the surface energy σ, in figure 17 the breakup frequency is also plotted as a function of $\mathscr{E} = 1/\mathscr{N}^2 = (6/\kappa)^2(\varrho a/\sigma)^2(R_g/a)^4\nu\langle\varepsilon\rangle$, similarly to what was done for the doublet.

Two asymptotic regimes for fast and slow breakup can be identified that obey power-law relationships:

$$f_{br}\tau_k \propto (1/\mathscr{N})^{\alpha} = \mathscr{E}^{\alpha/2}, \tag{4.2}$$

where the power-law exponent α can be fitted by numerical results. For given physical properties (ϱ, μ, σ) and particle size (a, R_g), these regimes also correspond to the limit of intense and weak turbulence, respectively. In the former one ($\alpha = 1$, and $\mathscr{E} \geqslant 100$, $\mathscr{N} \leqslant 0.1$), the turbulence is so intense that most of the fluctuations of the instantaneous strain rate lead to the rupture of the cluster. The mean breakup time $\langle\tau\rangle = 1/f_{br}$ is comparable to the Kolmogorov time scale, and hence to the characteristic frequency of the turbulent fluctuations of the smallest scales. By substituting the expressions for $\mathscr{E}$ and τ_k, the following relationship can be obtained for this regime:

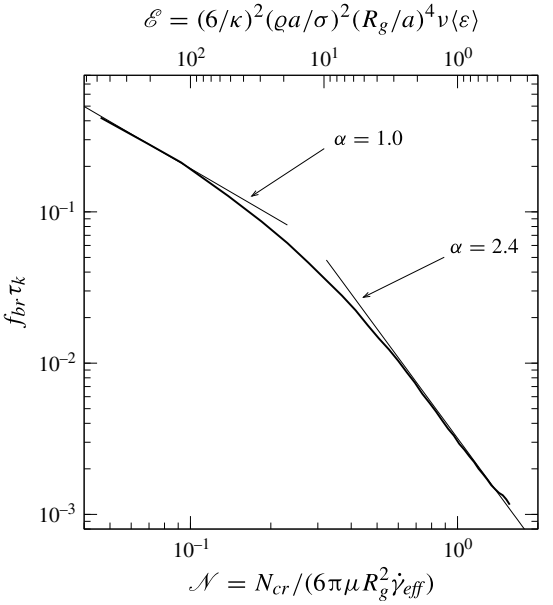

FIGURE 17. Breakage frequency of low-density isostatic CC aggregates.

$$f_{br} \propto \frac{\varrho a}{\sigma}\left(\frac{R_g}{a}\right)^2\langle\varepsilon\rangle, \tag{4.3}$$

showing that the breakup frequency is proportional to the mean turbulent dissipation rate, to the square of the aggregate size and to the inverse of the cohesive strength.

In the regime of weak turbulence ($\alpha = 2.4$, and $\mathscr{E} < 4$, $\mathscr{N} > 0.5$), the breakup frequency is small in comparison to the frequency of the smallest turbulent fluctuations and only the most intense peaks of shear rate are capable of breaking an aggregate. The breakup frequency is

$$f_{br} \propto \left(\frac{\varrho a}{\sigma}\right)^{2.4}\left(\frac{R_g}{a}\right)^{4.8}\nu^{0.7}\langle\varepsilon\rangle^{1.7} \tag{4.4}$$

and its increase with turbulence strength or particle size is much steeper than in the condition of fast breakup. Finally, a transition region, where α smoothly changes, separates the two extreme regimes. All of these regimes occur simultaneously in a stirred suspension, where particles of different size and regions of different dissipation rate are present. Consequently, as the variation of the power-law exponents between the regimes is large, the use of a single power-law relationship, such as (1.3), to characterise turbulent breakup in dilute suspensions is inadequate.

The cumulative distribution function for the size of the smaller of the two fragments formed by the breakup of 384-monomer aggregates is shown in figure 18, where the three curves refer to values of $\mathscr{E}$ equal to 10, 33 and 67. The cumulative fragment size distribution, $F(n_f)$, can be described satisfactorily as a function of the number of monomers in the smaller fragment n_f and the parent aggregate p:

$$\frac{F(n_f) - F_0}{1 - F_0} = 4\left(\frac{n_f}{p}\right)^2. \tag{4.5}$$

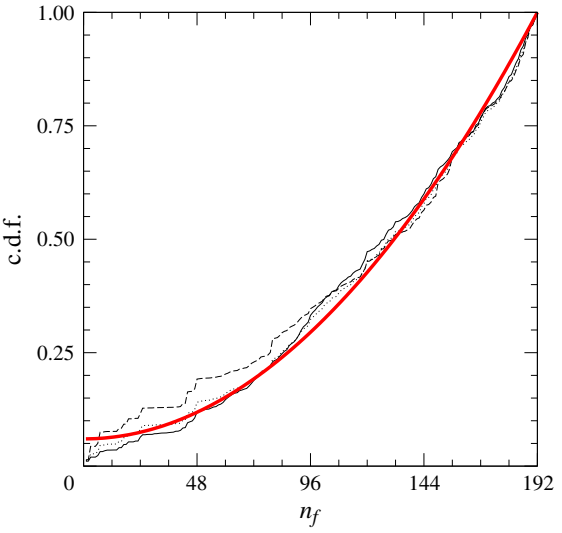

FIGURE 18. (Colour online) Cumulative distribution function for the number of monomers in the smaller of the two fragments formed by the breakup of 384-monomer aggregates ($D_f = 1.9$, $k_f = 1.2$): thick full line (red online), (4.5) with $F_0 = 0.06$; thin full line, $\mathscr{E} = 67$; dotted line, $\mathscr{E} = 33$; dashed line, $\mathscr{E} = 10$.

In this relationship, F_0 characterises the level of erosion, that is, of fragments formed by one or two monomers only. The formation of larger fragments (fragmentation) follows the quadratic function on the right-hand side of this equation. The difference among fragment distributions in the fast and intermediate regimes is quite small, and a single curve with F_0 around 5 % is capable of describing satisfactorily breakup in both regimes. In the slow breakup regime, a larger effect of erosion was observed. In this case, however, the number of sampled breakup events was much smaller than in the other two regimes. Although sufficient to evaluate a single parameter such as the breakup frequency, such a number was too small to give reliable estimation of the distribution function.

The adopted method tracks each cluster up to the start of breakup (the failure of the most stressed bond), and gives the breakup frequency and the size distribution of the fragments. When the formed fragments have moved away from each other, they behave as new independent particles, and their breakup frequency can be estimated again by first-passage-time statistics. The possibility of multiple fragmentation events, caused by the failure of additional bonds when the fragments are still so close to allow mutual interaction, cannot be taken into account by this approach. However, such a situation is not common for the considered aggregates. Their breakup normally leads to a large and sudden decrease in the maximum stress, because it occurs through the rupture of the filament where the effect of stress accumulation is largest. An exception could occur if different filaments with similar orientation and length, and consequently similar levels of stress, are simultaneously present in the aggregate, but, owing to the low solid density of our clusters, this is quite unlikely.

As discussed before, in previous studies the role of internal forces was neglected and it was assumed that an aggregate breaks up when the local instantaneous strain rate $\dot{\gamma}$ exceeds a critical value $\dot{\gamma}_{cr}$, which is a function only of the geometry and cohesive strength of the aggregate. In these studies, rupture does not depend on the

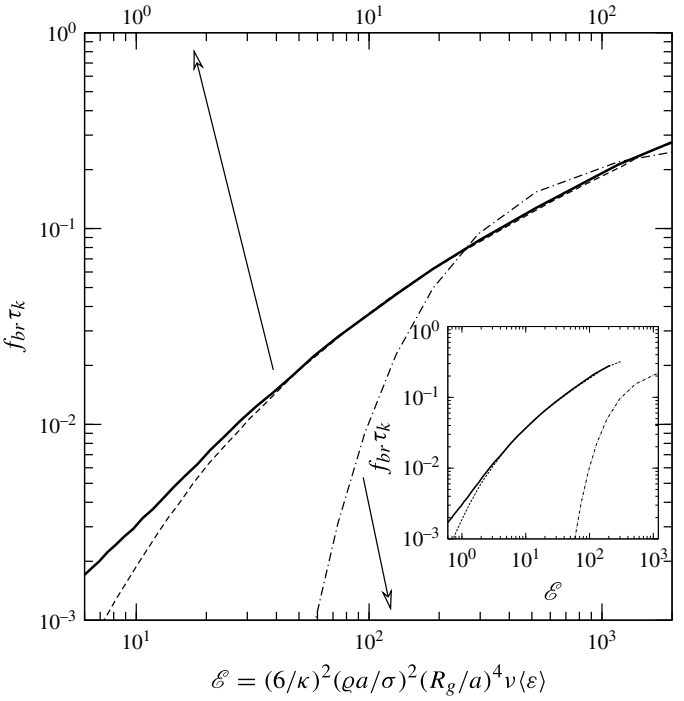

FIGURE 19. Comparison of the obtained breakup frequency (thick full line) with the results of the methods by Kusters (1991) (dot-dashed line) and Bäbler *et al.* (2012) (dashed line) using (4.6) to evaluate the critical shear rate. Two different horizontal scales are used: the lower one for the solution by Kusters, and the upper one for our results and the method by Baëbler *et al*. In the inset, the curves are plotted on one horizontal reference scale.

instantaneous orientation of the aggregate with respect to the local velocity gradient or the distribution of the strain among the different components of the gradient. Consequently, the critical shear rate for turbulent breakup can be determined by tests in pure laminar shear. The predictions of the methods based on this approach (Kusters 1991; Bäbler *et al.* 2012) are compared with our results in figure 19, using for $\dot{\gamma}_{cr}$ the following expression, which is based on a theoretical analysis of the breakup of isostatic CC aggregates in laminar shear flow (Vanni & Gastaldi 2011, equation (17)):

$$\dot{\gamma}_{cr} = c\frac{\kappa a\sigma}{\mu R_g^2}, \tag{4.6}$$

where c is a coefficient that depends on the morphology of the aggregates. To allow easier comparison with the results of the previous researchers, who related f_{br} to $\langle\varepsilon\rangle$, the breakage frequency is here plotted as a function of $\mathscr{E}$.

The expression (1.4) given by Kusters (1991) gives a very steep increase of the breakup frequency with the turbulence dissipation rate, followed by a sort of saturation of the process at larger $\langle\varepsilon\rangle$. The model assumes a normal distribution for velocity increments across the aggregate size and hence for $\dot{\gamma}$, which is significantly different from the nearly log-normal one observed in fully developed turbulent flows in experiments and DNS. It is probably a consequence of such inadequacy that,

when applied to the description of processes of aggregation–breakup conducted under a wide range of effective shear rates, Kusters' equation is often modified by substituting the critical shear rate $\dot{\gamma}_{cr}$, which should depend only on particle size, with an empirical function of both size and effective shear rate (Flesch, Spicer & Pratsinis 1999; Marchisio *et al.* 2006).

The first-passage-time method was proposed by Bäbler *et al.* (2012), and applied to the same set of turbulent trajectories as used for the present work. In the fast breakup region of $f_{br}\tau_k \approx 1$, where $\mathscr{N}$ is very small and $\mathscr{E}$ is large, both methods predict a linear relationship between f_{br} and $\langle\varepsilon\rangle$. In this regime, the turbulent fluctuations are so much larger than the critical value needed for rupture that they can break an aggregate even under unfavourable orientation, and thus the results of the two methods must coincide. Hence, in the regime of fast breakup, the effect of the orientation is negligible, and the obtained power-law behaviour, (4.3), recovers the result obtained without accounting for Stokesian dynamics. The coefficient c of (4.6) has no influence on the slope of the curve, but only shifts horizontally the solution given by Bäbler *et al.* (2012). In this case its value was set to $c = 0.9$ in order to impose the superposition of the two curves on the basis of the previous physical reasoning. The prescribed value is different, although not greatly, from the original one ($c = 1.4$) by Vanni & Gastaldi (2011). Such a difference, however, is probably a consequence of the use of a different set of clusters and a different method of extracting statistics between the present work and the paper by Vanni & Gastaldi.

In the slow breakage region of $f_{br}\tau_k \ll 1$ (characterised by large values of $\mathscr{N}$), the difference between the two approaches becomes relevant and the method of Bäbler *et al.* (2012) predicts a falloff of the breakup rate that is faster than the power-law prediction of (4.4). In this case fluctuations capable of breaking up an aggregate are rare and their strength does not normally exceed significantly the aggregate cohesion. In these situations, orientation becomes important for the outcome of the process in that, by proper alignment of the aggregate with the flow field, the internal stress at a bond may be enhanced or dampened.

The effect of the Reynolds number was not examined in this work. It is generally believed that the energy dissipation rate goes to a finite limit as Reynolds number goes to infinity. This is supported by a number of experimental observations, and generally accepted from a theoretical point of view (Frisch 1995; Sreenivasan & Antonia 1997). Moments of the energy dissipation depend on the Reynolds number as power laws, with scaling exponents that are thought to be universal for isotropic and homogeneous turbulence (and independent of Reynolds number). However, these exponents are measured to be extremely small, so a Reynolds-number dependence of the breakup rate could well exist, but we expect it to be small or vanishing.

Real aggregates, with features similar to those of the model aggregates examined so far (i.e. isostatic clusters of low fractal dimension), are normally obtained by aggregation of highly destabilised colloidal suspensions, in which all collisions lead to a permanent bond and no restructuring of the structures has occurred (Vanni 2000*b*). Since the generation method of such aggregates proceeds through the sequential addition of smaller clusters to a growing aggregate without any restructuring, the obtained structure is isostatic and made mostly of filaments of primary particles, attached at one end and without internal loops. In these systems the viscous stresses that cause breakup also cause the restructuring of the aggregates, by making their structure more compact and hyperstatic. Hence, the above analysis is only applicable to the initial steps of a breakup process, when the role of restructuring is still negligible.

The effect of a hyperstatic structure on breakup depends on the level of overconstrainment. Highly hyperstatic aggregates show a strongly cross-linked structure, in which the hydrodynamic force acting on a monomer is distributed on its numerous contacting neighbours and discharged locally, instead of being propagated along chains of particles. This feature makes the internal stress distribution and the mechanism of breakup very different with respect to those of isostatic clusters. Preliminary work based on the adoption of a linear stress–strain relationship for contact deformations (Vanni 2014) shows indeed that in this case the maximum stress is always located at the periphery of the aggregate, where the largest hydrodynamic force is applied. The process of breakup is more complex in this case, since the failure of the bond with the largest stress may give rise to different outcomes: simple redistribution of internal stresses because of the redundancy of links; direct generation of a small fragment at the periphery of the aggregate; start of a sequence of failures of inter-monomer links that eventually form a crack and split the aggregate into fragments. On the contrary, in weakly hyperstatic aggregates, the mechanism of transmission and propagation of internal stresses along chains of particles is retained. The strength of the internal stress for these structures and, consequently, the breakup frequency are smaller in comparison to isostatic clusters, since the weakest bonds are removed by the restructuring process, but we expect the qualitative features concerning spatial distribution of stress, size of fragments and breakup regimes to be similar, because of the preservation of the filamentous structure.

5. Conclusions

By characterising the stresses generated by homogeneous isotropic turbulence in rigid aggregates, we estimated theoretically the rate of turbulent breakup of colloidal aggregates and the size distribution of the formed fragments. We examined isostatic aggregates, in which the failure of a single contact causes the rupture of the aggregate. It is likely that most of the features of such particles are retained also by weakly hyperstatic aggregates. On the contrary, highly compact and overconstrained clusters have a very different response to the hydrodynamic flow field, leading to a more complex mechanism of breakup, which may occur by nucleation and propagation of cracks and cannot be captured by the present analysis.

For a given aggregate, the internal stresses depend on the instantaneous flow field around the aggregate and its orientation with respect to the flow, which, in turn, depends on the Lagrangian history of the particle. As a consequence, the translational and rotational motion of the aggregate needs to be tracked. We considered two classes of particles, namely doublets and low-density large isostatic aggregates. Doublets show the highest sensitivity to the effect of orientation on breakup, as it is the orientation that determines if their inter-monomer contact is under traction or compression. Hence, since the failure of a contact is caused by a tensile stress, breakup can only occur if the doublet shows a favourable alignment with respect to the flow field. On the contrary, in large and highly disordered aggregates, there are contacts under traction for any spatial configuration. Therefore, these aggregates can be broken under most orientations, provided that the strength of the strain rate is large enough. Clearly in this case the effect of orientation is much smaller, but nevertheless still significant, especially for conditions of slow breakup.

Asymptotic regimes with limiting laws have been found for the two cases in which the time-averaged stresses induced in the solid by turbulence are much larger or much smaller than the cohesive strength of the aggregate, corresponding to the conditions of

fast and slow breakup, respectively. For large aggregates these limiting relationships have a power-law form and become particularly simple for the fast breakup region, where the breakup frequency is proportional to the mean turbulent dissipation rate, the square of aggregate size and the inverse of the cohesive strength. For such aggregates it has been confirmed that the proper scaling length for maximum stress and breakup is the radius of gyration. The cumulative fragment distribution function is nearly independent of the mean turbulent dissipation and can be approximated by the sum of a small erosive component and a term that is quadratic with respect to fragment size.

Acknowledgements

Support from the EU COST Action MP0806 'Particles in Turbulence' for A.S.L. and M.V. is acknowledged. We thank CINECA Super Computing Centre (Italy), for hosting the iCFD database and for technical support.

REFERENCES

ADLER, P. M. & MILLS, P. M. 1979 Motion and rupture of a porous sphere in a linear flow field. *J. Rheol.* **23**, 25–38.

ANDERSON, E., BAI, Z., BISCHOF, C., BLACKFORD, S., DEMMEL, J., DONGARRA, J., DU CROZ, J., GREENBAUM, A., HAMMARLING, S., MCKENNEY, A. & SORENSEN, D. 1999 *LAPACK Users' Guide*, 3rd edn. SIAM.

BÄBLER, M. U., BIFERALE, L. & LANOTTE, A. S. 2012 Breakup of small aggregates driven by turbulent hydrodynamical stress. *Phys. Rev.* E **85**, 025301.

BÄBLER, M. U., MORBIDELLI, M. & BALDYGA, J. 2008 Modelling the breakup of solid aggregates in turbulent flows. *J. Fluid Mech.* **612**, 261–289.

BACHE, D. H. 2004 Floc rupture and turbulence: a framework for analysis. *Chem. Engng Sci.* **59**, 2521–2534.

BEC, J., BIFERALE, L., CENCINI, M., LANOTTE, A. S. & TOSCHI, F. 2010*a* Intermittency in the velocity distribution of heavy particles in turbulence. *J. Fluid Mech.* **646**, 527–536.

BEC, J., BIFERALE, L., LANOTTE, A. S., SCAGLIARINI, A. & TOSCHI, F. 2010*b* Turbulent pair dispersion of inertial particles. *J. Fluid Mech.* **645**, 497–528.

BECKER, V., SCHLAUCH, E., BEHR, M. & BRIESEN, H. 2009 Restructuring of colloidal aggregates in shear flows and limitations of the free-draining approximation. *J. Colloid Interface Sci.* **339**, 362–372.

BOSSIS, G., MEUNIER, A. & BRADY, J. F. 1991 Hydrodynamic stress on fractal aggregates of spheres. *J. Chem. Phys.* **94**, 5064–5070.

BRADY, J. F. & BOSSIS, G. 1988 Stokesian dynamics. *Annu. Rev. Fluid Mech.* **20**, 111–157.

BRETHERTON, F. P. 1962 The motion of rigid particles in a shear flow at low Reynolds numbers. *J. Fluid Mech.* **14**, 284–304.

CALVERT, G., GHADIRI, M. & TWEEDIE, R. 2009 Aerodynamic dispersion of cohesive powders: a review of understanding and technology. *Adv. Powder Technol.* **20**, 4–16.

CARPICK, R. W., OGLETREE, D. F. & SALMERON, M. 1999 A general equation for fitting contact area and friction vs load measurements. *Adv. Colloid Interface Sci.* **211**, 395–400.

DELICHATSIOS, M. A. 1975 Model for the breakup rate of spherical drops in isotropic turbulent flows. *Phys. Fluids* **18**, 622–623.

DELICHATSIOS, M. A. & PROBSTEIN, R. F. 1976 The effect of coalescence on the average drop size in liquid–liquid dispersions. *Ind. Engng Chem. Fundam.* **15**, 134–138.

DERKSEN, J. J. 2008 Flow-induced forces in sphere doublets. *J. Fluid Mech.* **608**, 337–356.

DUKHIN, S., ZHU, C., DAVE, R. N. & YU, Q. 2005 Hydrodynamic fragmentation of nanoparticle aggregates at orthokinetic coagulation. *Adv. Colloid Interface Sci.* **114–115**, 119–131.

DURLOFSKY, L., BRADY, J. F. & BOSSIS, G. 1987 Dynamic simulation of hydrodynamically interacting particles. *J. Fluid Mech.* **180**, 21–49.

EGGERSDORFER, M. L., KADAU, D., HERRMANN, H. J. & PRATSINIS, S. E. 2010 Fragmentation and restructuring of soft agglomerates under shear. *J. Colloid Interface Sci.* **342**, 261–268.

FANELLI, M., FEKE, D. L. & MANAS-ZLOCZOWER, I. 2006 Prediction of the dispersion of particle clusters in the nano-scale – part I: steady shearing responses. *Chem. Engng Sci.* **61**, 473–488.

FILIPPOV, A. V., ZURITA, M. & ROSNER, D. E. 2000 Fractal-like aggregates: relation between morphology and physical properties. *J. Colloid Interface Sci.* **229**, 261–273.

FLESCH, J. C., SPICER, P. T. & PRATSINIS, S. E. 1999 Laminar and turbulent shear-induced flocculation of fractal aggregates. *AIChE J.* **45**, 1114–1124.

FRISCH, U. 1995 *Turbulence: The Legacy of A. N. Kolmogorov*. Cambridge University Press.

GASTALDI, A. & VANNI, M. 2011 The distribution of stresses in rigid fractal-like aggregates in a uniform flow field. *J. Colloid Interface Sci.* **357**, 18–30.

GOLDSTEIN, H., POOLE, C. & SAFKO, J. 1983 *Classical Mechanics*, 3rd edn. Addison-Wesley.

GUAZZELLI, E. & MORRIS, J. F. 2012 *A Physical Introduction to Suspension Dynamics*. Cambridge University Press.

HARADA, S., TANAKA, R., NOGAMI, H. & SAWADA, M. 2006 Dependence of fragmentation behaviour of colloidal aggregates on their fractal structure. *J. Colloid Interface Sci.* **301**, 123–129.

HARSHE, Y. M., EHRL, L. & LATTUADA, M. 2010 Hydrodynamic properties of rigid fractal aggregates of arbitrary morphology. *J. Colloid Interface Sci.* **352**, 87–98.

HARSHE, Y. M. & LATTUADA, M. 2012 Breakage rate of colloidal aggregates in shear flow through Stokesian dynamics. *Langmuir* **28**, 283–292.

HIGASHITANI, K. & IIMURA, K. 1998 Two-dimensional simulation of the breakup process of aggregates in shear and elongational flows. *J. Colloid Interface Sci.* **204**, 320–327.

HIGASHITANI, K., IIMURA, K. & SANDA, H. 2001 Simulation of deformation and breakup of large aggregates in flows of viscous fluids. *Chem. Engng Sci.* **56**, 2927–2938.

HORWATT, S. W., FEKE, D. L. & MANAS-ZLOCZOWER, I. 1992*a* The influence of structural heterogeneities on the cohesivity and breakup of agglomerates in simple shear flow. *Powder Technol.* **72**, 113–119.

HORWATT, S. W., MANAS-ZLOCZOWER, I. & FEKE, D. L. 1992*b* Dispersion behaviour of heterogeneous agglomerates at supercritical stresses. *Chem. Engng Sci.* **47**, 1849–1855.

ICHIKI, K., KOBRYN, A. E. & KOVALENKO, A. 2008 Targeting transport properties in nanofluidics: hydrodynamic interaction among slip surface nanoparticles in solution. *J. Comput. Theor. Nanosci.* **5**, 2004–2021.

JOHNSON, K. L. 1985 *Contact Mechanics*. Cambridge University Press.

KOBAYASHI, M., ADACHI, Y. & DOI, S. 1999 Breakup of fractal flocs in a turbulent flow. *Langmuir* **15**, 4351–4356.

KUSTERS, K. A. 1991 On aggregation of small particles in agitated vessels. PhD thesis, Chemical Engineering, Technische Universiteit Eindhoven.

LU, C. F. & SPIELMAN, L. A. 1985 Kinetics of floc breakage and aggregation in agitated liquid suspensions. *J. Colloid Interface Sci.* **103**, 95–105.

MANAS-ZLOCZOWER, I. & FEKE, D. 2009 Dispersive mixing of solid additives. In *Mixing and Compounding of Polymers: Theory and Practice* (ed. I. Manas-Zloczower), pp. 183–216. Hanser.

MARCHISIO, D. L. & FOX, R. O. 2013 *Computational Models for Polydisperse Particulate and Multiphase Systems*. Cambridge University Press.

MARCHISIO, D., SOOS, M., SEFCIK, J. & MORBIDELLI, M. 2006 Role of turbulent shear rate distribution in aggregation and breakage processes. *AIChE J.* **52**, 158–173.

MAUGIS, D. 1992 Adhesion of spheres: the JKR–DMT transition using a Dugdale model. *J. Colloid Interface Sci.* **150**, 243–269.

NIR, A. & ACRIVOS, A. 1973 On the creeping motion of two arbitrary-sized touching spheres in a linear shear field. *J. Fluid Mech.* **59**, 209–223.

PANDYA, J. D. & SPIELMAN, L. A. 1983 Floc breakage in aggregate suspensions: effect of agitation rate. *J. Colloid Interface Sci.* **38**, 1983–1992.

PARKER, D. S., KAUFMANN, W. J. & JENKINS, J. 1972 Floc breakup in turbulent flocculation processes. *Proc. Am. Soc. Civil Engnrs, J. Sanitary Engng Div.* **98**, 79–99.

PARSA, S., CALZAVARINI, E., TOSCHI, F. & VOTH, G. A. 2012 Rotation rate of rods in turbulent fluid flow. *Phys. Rev. Lett.* **109**, 134501.

POTANIN, A. A. 1993 On the computer simulation of the deformation and breakup of colloidal aggregates in shear flow. *J. Colloid Interface Sci.* **157**, 399–410.

PUMIR, A. & WILKINSON, M. 2011 Orientation statistics of small particles in turbulence. *New J. Phys.* **13**, 093030.

REDNER, S. 2001 *A Guide to First Passage Processes*. Cambridge University Press.

SANCHEZ FELLAY, L. & VANNI, M. 2012 The effect of flow configuration on hydrodynamic stresses and dispersion of low density rigid aggregates. *J. Colloid Interface Sci.* **388**, 47–55.

SETO, R., BOTET, R. & BRIESEN, H. 2011 Hydrodynamic stress on small colloidal aggregates in shear flow using Stokesian dynamics. *Phys. Rev.* E **84**, 041405.

SONNTAG, R. C. & RUSSEL, W. B. 1987 Structure and breakup of flocs subjected to fluid stresses. II. Theory. *J. Colloid Interface Sci.* **115**, 378–389.

SORENSEN, C. M. & ROBERTS, G. C. 1997 The prefactor of fractal aggregates. *J. Colloid Interface Sci.* **186**, 447–452.

SPICER, P. T. & PRATSINIS, S. E. 1996 Coagulation and fragmentation: universal steady-state particle-size distribution. *AIChE J.* **42**, 1612–1620.

SREENIVASAN, K. R. & ANTONIA, R. A. 1997 The phenomenology of small-scale turbulence. *Annu. Rev. Fluid Mech.* **29**, 435–472.

TADMOR, Z. 1976 Forces in dispersive mixing. *Ind. Engng Chem. Fundam.* **15**, 346–348.

THOUY, R. & JULLIEN, R. 1994 A cluster–cluster aggregation model with tunable fractal dimension. *J. Phys. A: Math. Gen.* **27**, 2953–2963.

VANNI, M. 2000*a* Approximate population balance equations for aggregation–breakage processes. *J. Colloid Interface Sci.* **221**, 243–260.

VANNI, M. 2000*b* Creeping flow over spherical permeable aggregates. *Chem. Engng Sci.* **55**, 685–698.

VANNI, M. 2014 Internal stresses and breakup of porous aggregates in homogeneous isotropic turbulence. In *ASME 2014 4th Joint US–European Fluids Engineering Division Summer Meeting*, Paper FEDSM2014-21558.

VANNI, M. & GASTALDI, A. 2011 Hydrodynamic forces and critical stresses in low-density aggregates under shear flow. *Langmuir* **27**, 12822–12833.

WENGELER, R. & NIRSCHL, H. 2007 Turbulent hydrodynamic stress induced dispersion and fragmentation of nanoscale agglomerates. *J. Colloid Interface Sci.* **306**, 262–273.

ZACCONE, A., SOOS, M., LATTUADA, M., WU, H., BÄBLER, M. & MORBIDELLI, M. 2009 Breakup of dense colloidal aggregates under hydrodynamic stresses. *Phys. Rev.* E **79**, 061401.